Wide-field imaging with Hyper Suprime-Cam: Cosmology and Galaxy Evolution

A Strategic Survey Proposal for the Subaru Telescope

PI: Satoshi Miyazaki (NAOJ)
Co-PI: Ikuru Iwata (NAOJ)

The HSC collaboration team[1]: S. Abe[1], H. Aihara[⋆,2,3], M. Akiyama[4], K. Aoki[5], N. Arimoto[⋆,5], N. A. Bahcall[6], S. J. Bickerton[3], J. Bosch[6], K. Bundy[†,3], C. W. Chen[7], M. Chiba[†,4], T. Chiba[8], N. E. Chisari[6], J. Coupon[7], M. Doi[2], M. Enoki[9] S. Foucaud[10], M. Fukugita[3], H. Furusawa[†,5], T. Futamase[4], R. Goto[2], T. Goto[11], J. E. Greene[6], J. E. Gunn[†,6], T. Hamana[†,5], T. Hashimoto[2], M. Hayashi[5], Y. Higuchi[2,5], C. Hikage[12], J. C. Hill[6], P. T. P. Ho[⋆,7], B. C. Hsieh[7], K. Y. Huang[†,7], H. Ikeda[13], M. Imanishi[5], N. Inada[14], A. K. Inoue[15], W.-H. Ip[1], T. Ito[5], K. Iwasawa[16], M. Iye[5], H. Y. Jian[17], Y. Kakazu[18], H. Karoji[3], N. Kashikawa[5], N. Katayama[3], T. Kawaguchi[19], S. Kawanomoto[5], I. Kayo[20], T. Kitayama[20], G. R. Knapp[6], T. Kodama[5], K. Kohno[2], M. Koike[5], E. Kokubo[5], M. Kokubo[2], Y. Komiyama[5], A. Konno[2], Y. Koyama[5], C. N. Lackner[3], D. Lang[6], A. Leauthaud[†,3], M. J. Lehner[7], K.-Y. Lin[7], L. Lin[7], Y.-T. Lin[†,7], C. P. Loomis[6], R. H. Lupton[†,6], P. S. Lykawka[21], K. Maeda[3], R. Mandelbaum[†,22], Y. Matsuda[5], K. Matsuoka[13,23], Y. Matsuoka[12], S. Mineo[2], T. Minezaki[2], H. Miyatake[6], R. Momose[2], A. More[3], S. More[3], T. J. Moriya[3], T. Morokuma[†,2], H. Murayama[⋆,3], K. Nagamine[24], T. Nagao[†,23], S. Nagataki[23], Y. Naito[2], K. Nakajima[2], F. Nakata[5], H. Nakaya[5], T. Namikawa[2], C.-C. Ngeow[1], T. Nishimichi[3], H. Nishioka[7], A. J. Nishizawa[†,3], K. Nomoto[3], M. Oguri[†,3], A. Oka[2], N. Okabe[7], S. Okamoto[25], S. Okamura[26], J. Okumura[23], S. Okumura[27], Y. Okura[5], Y. Ono[2] M. Onodera[28], K. Ota[23], M. Ouchi[†,2], S. Oyabu[12], P. A. Price[6], R. Quimby[3], C. E. Rusu[2,5], S. Saito[29], T. Saito[3], Y. Saitou[30], M. Sato[12], T. Shibuya[5], K. Shimasaku[†,2], A. Shimono[3], S. Shinogi[2], M. Shirasaki[2], J. D. Silverman[3], D. N. Spergel[⋆,6,3], M. A. Strauss[†,6], H. Sugai[3], N. Sugiyama[12,3], D. Suto[2], Y. Suto[⋆,2], K. Tadaki[2], M. Takada[†,3], R. Takahashi[31], S. Takahashi[5], T. Takata[5], T. T. Takeuchi[12], N. Tamura[3], M. Tanaka[5], M. Tanaka[†,3], M. Tanaka[4], Y. Taniguchi[13], A. Taruya[2], T. Terai[5], Y. Terashima[13], N. Tominaga[32], J. Toshikawa[30], T. Totani[23], M. Tsai[1], E. L. Turner[⋆,6], Y. Ueda[23], K. Umetsu[7], Y. Urata[†,1], Y. Utsumi[5], B. Vulcani[3], K. Wada[33], S.-Y. Wang[7], W.-H. Wang[7], T. Yamada[4], Y. Yamada[5], K. Yamamoto[34], H. Yamanoi[5], C.-H. Yan[7], N. Yasuda[†,3], A. Yonehara[35], F. Yoshida[†,5], N. Yoshida[2], M. Yoshikawa[36], S. Yuma[2] (1) NCU, Taiwan (2) Tokyo (3) Kavli IPMU (4) Tohoku (5) NAOJ (6) Princeton (7) ASIAA (8) Nihon (9) Tokyo Keizai (10) NTNU, Taiwan (11) DARK, Copenhagen (12) Nagoya (13) Ehime (14) NNCT (15) Osaka Sangyo (16) Barcelona (17) NTU, Taiwan (18) Chicago (19) Tsukuba (20) Toho (21) Kinki (22) CMU (23) Kyoto (24) Las Vegas (25) KIAA, China (26) Hosei (27) JSGA (28) ETH (29) Berkeley (30) GUAS (31) Hirosaki (32) Konan (33) Kagoshima (34) Hiroshima (35) Kyoto Sangyo (36) JAXA

Executive Summary

We propose to carry out a three-layered, multi-band (*grizy* plus narrow-band filters) imaging survey with the Hyper Suprime-Cam (HSC) on the 8.2m Subaru Telescope. By combining data from the three layers (Wide: 1400 deg^2, $r \simeq 26$; Deep: 27 deg^2, $r \simeq 27$; Ultradeep: 3.5 deg^2, $r \simeq 28$), we will address some of the most pressing problems in modern cosmology and astrophysics: the origin of the acceleration of the Universe's expansion, the properties and evolution of galaxies from $z \simeq 7$ to today, and the nature of cosmic reionization. The survey is uniquely designed to enable all these science cases, with particular attention to controlling systematic errors, and the data will be analyzed with a state-of-the-art software pipeline. We will use the excellent-quality ($0.7''$ seeing), multi-broadband images of distant galaxies from the Wide layer to statistically reconstruct the dark matter distribution in the Universe up to $z \simeq 1.5$ via measurements of weak lensing (WL), coupled with photometric redshifts for every galaxy. The Deep layer goes one magnitude deeper, with repeated observations, allowing us to verify our PSF and galaxy shape measurements as a function of seeing, depth and galaxy properties. Measurements of cosmic shear and other HSC WL observables, in combination with geometrical constraints from lightcurves of ~ 120 Type Ia supernovae up to $z \simeq 1.4$ from the Ultradeep layer, will enable us to constrain the dark energy parameters to precisions of $\sigma(w_{\rm DE}) \simeq 0.04$ (constant dark energy equation of state) and the dark energy figure-of-merit ${\rm FoM} \equiv 1/[\sigma(w_{\rm pivot})\sigma(w_a)] \simeq 50$ (for $w(z)$ a two-parameter function of redshift), about a factor of 2 improvement over current constraints. Cross-correlating the HSC WL observables with data from the arcminute-resolution, high-sensitivity ACT CMB experiment, Planck, and the SDSS/BOSS spectroscopic galaxy survey will improve the FoM to 100. We will also perform a stringent test of gravity on cosmological distance scales by comparing dark matter clustering from HSC-WL observables with the redshift-space distortion effect measured in the BOSS galaxy clustering. In the field of galaxy evolution, the HSC survey will include over 20 million galaxies up to $z \simeq 1$ from the Wide layer, and a half-million galaxies over $1 \lesssim z \lesssim 2$ from the Deep and Ultradeep layers. These galaxy catalogs, of unprecedented sizes and cosmological volumes, will allow high-precision measurements of the properties of evolving galaxy populations and their relation to the WL-reconstructed dark matter distribution. With samples constructed from the Wide layer, we will measure absolute stellar growth rates over 2 orders of magnitude in stellar mass since $z \sim 1$, and establish evolutionary links between galaxy populations by tracking how the growth of some key sub-populations is related to the decline of others. A growth rate of 3% per Gyr will be measured with 10σ or greater precision across all mass bins probed. The Deep and Ultradeep layers will also include broad- and narrow-band imaging surveys of Lyman-break galaxies

[1]Those people with the "⋆" superscript are the HSC Executive Board members. Those people with the "†" superscript are co-chairs of the HSC working groups (Weak Lensing, AGN, Galactic Structure, Solar System, Variables/Transients, Low-z Galaxies, High-z Galaxies, Clusters, Photometric Redshift, Photometric Calibration, Survey Strategy, Hardware, and Software & Data Distribution).

(LBGs), Lyman-α emitters (LAEs) and quasars to an unprecedented depth and solid angle. The clustering of the LBG samples will allow us to determine the dependence of the stellar mass and star formation rate on the host dark halo mass over $M_{\rm halo} \sim 10^{11} - 10^{13} M_\odot$ in the era of galaxy formation, $z \sim 2 - 7$. We will measure the clustering and luminosity functions of LAEs at $z = 2.2$, 5.7, 6.6, and 7.3 with samples extending down to $\sim 0.3L^*$. At high redshift, these will allow us to constrain the neutral hydrogen fraction of the intergalactic medium, $x_{\rm HI}$, at $z \sim 7$ with a precision of $\sigma(x_{\rm HI}) \sim 0.1$, and to constrain the topology of spatially-inhomogeneous reionization.

1 Introduction

We live in a golden age for extragalactic astronomy and cosmology. We now have a quantitative and highly predictive model for the overall composition and expansion history of the Universe that is in accord with a large array of independent and complementary observations. Observations of galaxies over most of the 13.7 billion year history of the Universe have led to a broad-brush understanding of the basics of galaxy evolution. However, there are fundamental and inter-related questions that remain:

- What is the physical nature of dark matter and dark energy? Is dark energy truly necessary, or could the accelerated expansion of the Universe be explained by modifications of the law of gravity?
- How did galaxies assemble, and how did their properties change, over cosmic time?
- What is the topology and timing of reionization at high redshift? What were the ionizing sources?

These questions, and many more, can be addressed with a comprehensive deep and wide-angle imaging survey of the sky, using the Hyper Suprime-Cam (HSC) on the 8.2m Subaru Telescope. The combination of the large aperture of the Subaru Telescope, the large field of view (1.77 deg^2) of HSC, and the excellent image quality of the site and the telescope make this the ideal instrument for addressing these fundamental questions in modern cosmology and astronomy. We propose a 300-night strategic survey program, involving astronomers from Japan, Taiwan, and Princeton University in the United States. The survey will consist of three layers, which together will explore galaxy evolution over the full range of cosmic history from the present to redshift 7, probing both starlight (from the photometry) and dark matter (using gravitational lensing). The weak lensing (WL) allows us to measure the large-scale distribution of dark matter and its evolution with cosmic time. Cross-correlations of HSC WL observables with the spectroscopic galaxy distribution in the SDSS/Baryon Oscillation Spectroscopic Survey (BOSS) and the observed temperature and polarization fluctuations in the Cosmic Microwave Background (CMB) will constrain the parameters of the standard model of cosmology, and test for exotic variations such as deviations from the predictions of General Relativity on cosmological scales. Studies of the highest-redshift galaxies and quasars discovered in this survey will lead to a deeper understanding of reionization, a key event in the thermal history of the Universe.

Table 1: **Summary of HSC-Wide, Deep and Ultradeep layers**

Layer	Area [deg^2]	# of HSC fields	Filters & Depth	Comoving volume [h^{-3}Gpc^3]	Key Science
Wide	1400	916	*grizy* ($r \simeq 26$)	$\sim 4.4\,(z < 2)$	WL cosmology, $z \sim 1$ gals, clusters
Deep	27	15	*grizy*+3NBs ($r \simeq 27$)	$\sim 0.5\,(1 < z < 5)$	$z \lesssim 2$ gals, reionization, WL calib.
Ultradeep	3.5	2	*grizy*+3NBs ($r \simeq 28$)	$\sim 0.07\,(2 < z < 7)$	$z \gtrsim 2$ gals, reionization, SNeIa

The experience of the Sloan Digital Sky Survey (SDSS; York et al. 2000), and the tremendous success of the current prime-focus camera on Subaru, Suprime-Cam (Miyazaki et al. 2002a), have demonstrated the power of wide-field imaging to make science breakthroughs in a broad range of topics. The SDSS imaged in five broad-bands (u, g, r, i, and z), to a depth of $r \approx 22.5$ (5σ point source). It has produced more highly cited papers in recent years than any other observational facility, including the Keck Telescopes and the *Hubble Space Telescope* (Madrid & Macchetto 2009). The SDSS characterized the nature and distribution of galaxies in the local present-day Universe. Observations with Suprime-Cam have led the world in studies of the distant Universe, and have shown that an imager on the Subaru telescope has the potential to extend SDSS low-redshift discoveries in the field of cosmology and galaxy formation/evolution to the intermediate- and high-redshift Universe. The HSC survey we propose will cover SDSS-like volumes at high redshift, making it the first truly large-scale survey of the distant Universe.

The **top-level scientific goals** for the HSC survey are:

- To derive stringent dark energy constraints from the combination of the HSC WL observables and the galaxy clustering information from the BOSS survey to precisions of $\sigma(w_{\rm pivot}) \simeq 0.03$ and the dark energy

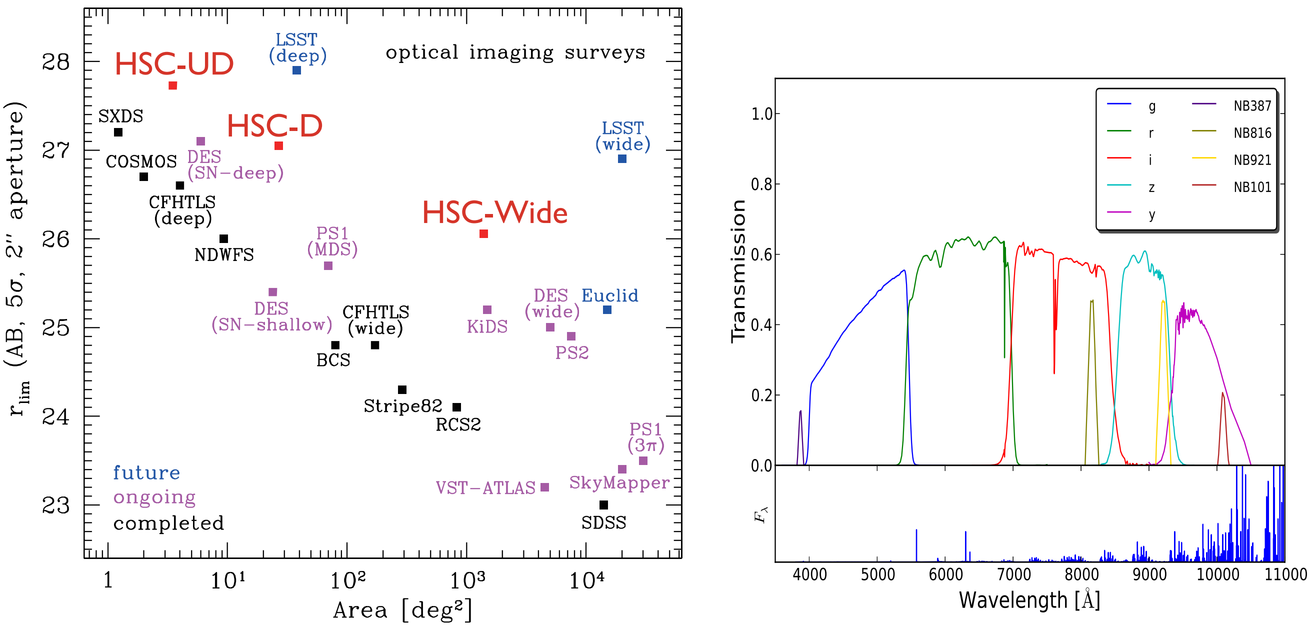

Figure 1: *Left*: The limiting magnitudes (in r) and solid angles of the HSC-Wide, Deep and Ultradeep (UD) layers, compared with other existing, on-going, and planned surveys. The three layers are complementary to each other, and each of the three layers covers a significantly wider area than do other on-going surveys of comparable depth. The narrow-band components of the Deep and Ultradeep layers are unique; no other project is planning a major survey to comparable depth. *Right*: The HSC bandpasses, including the reflectivity of all mirrors, transmission of all optics and filters, and response of the CCDs, assuming an airmass of 1.1. Both the broad-band and narrow-band filters are shown. The lower panel shows the spectrum of sky emission lines, demonstrating that the red narrow-band filters lie in relatively dark regions of the sky spectrum.

figure-of-merit FoM $\equiv 1/[\sigma(w_{\rm pivot})\sigma(w_a)] \simeq 100$.

- To use WL to constrain deviations from General Relativity to a higher precision than the current SDSS constraint (Reyes, Mandelbaum et al. 2010) by a factor of 4.
- To study SDSS-like volumes of galaxies in a series of redshift slices observed through broad- and narrow-band filters to carefully-tuned depths, in order to understand the properties and evolution of galaxies from $z \sim 7$ to today, as well as to constrain the physics of cosmic reionization at high redshift, $z \simeq 5-7$.

To achieve these scientific goals, we propose a 'wedding-cake' survey with three layers:

- The Wide layer will cover 1400 deg^2 and will be done in five broad-bands, g, r, i, z, and y, to a depth of $r \simeq 26$, and to similar depths in the other bands. This is designed to characterize the $z < 2$ galaxy population, and to measure WL shear as a function of redshift and spatial scale.
- The Deep layer will cover 27 deg^2 in four carefully selected fields distributed over a range of right ascensions (RA). It will go a magnitude deeper than the Wide layer in the broad-bands, and will also use three narrow-band filters to look for Lyman-α emitters (LAEs) at $z = 2.2$, 5.7, and 6.6 to study their evolution and the topology of cosmic reionization. Its multiple repeat exposures will enable powerful testing and mitigation of systematic lensing errors.
- The Ultradeep (UD) layer will image two fields (3.5 deg^2) in both the five broad-band filters and three narrow-band filters, going a magnitude fainter still, to discover ~ 6000 LAEs at $z = 5.7$ and 6.6, several tens of LAEs at $z = 7.3$, and about 120 Type Ia supernovae to $z \sim 1.4$.

The left panel of Figure 1 shows that these three layers are complementary to each other and are significantly more powerful than are the previous, competitive on-going, and upcoming surveys. Combining the three layers allows us to cover a broad range of science topics spanning a wide range of length scales and redshifts. We need about 200 nights in total (including overheads and assuming that 30% of nights will have poor weather) to carry out the Wide layer, and 100 nights for the Deep and Ultradeep layers. Table 1 summarizes the survey parameters and main science drivers for each layer.

Our two scientific themes, cosmology and galaxy evolution, are intimately tied together, which is why we tackle both under a single survey program. Using WL for cosmology requires detailed knowledge of the photometric properties of galaxies, including their intrinsic shapes and spectral energy distributions in order to measure photometric redshifts. Conversely, one needs to understand galaxy evolution in a cosmological context, and tighter constraints on cosmological models allow a better theoretical understanding of how galaxy formation takes place. In order to use galaxies and their spatial distribution as a cosmological probe, we need to understand the dark matter halos in which they live, which we can probe with galaxy-galaxy and cluster-galaxy weak lensing. Each of the Wide, Deep, and Ultradeep layers contributes to both our cosmology and galaxy evolution studies in a fundamental way.

Our proposed survey will be the largest program ever carried out with Subaru, both in terms of the number of nights and the volume of data. This is a community-driven survey, with broad support in the Japanese community. Following the example of the SDSS collaboration, we have developed a sophisticated image processing pipeline and a clear management structure to operate the survey and promote the international collaboration. Based on the expertise we will establish with this HSC survey program, we, led by the HSC project office at NAOJ, will support observations and data analysis with HSC for the community, including open-use programs.

The next five years is the optimal time to carry out this survey. While there are several other major imaging surveys being undertaken around the world, with related science goals (Pan-STARRS, Dark Energy Survey (DES) on the CTIO 4m telescope, the KIlo-Degree Survey (KIDS) on the 2.6m VST, and SkyMapper are the most prominent; see Figure 1 for details), none is being done on a telescope as large, and as high-quality, as Subaru. The product of primary mirror collecting area and field of view of HSC (the étendue) is the highest of any instrument in the world, and will continue to be so until the next decade (2020 era), when even larger imaging surveys such as the Large Synoptic Survey Telescope (LSST) on the ground and the satellite missions Euclid (ESA) and WFIRST (NASA) see first light. The survey we propose will be a precursor survey to those projects, with related science goals and similar depth, and thus will place Japanese astronomy in a leadership role in the field into the next decade. It will also provide discoveries and object lists that will be used for a wide-field multi-object Prime Focus Spectrograph (PFS) planned for Subaru, as well as the Thirty Meter Telescope.

After a brief description of the HSC instrument itself (Section 2), we describe our core science goals in cosmology (Section 3), and galaxy evolution and cosmic reionization (Sections 4 and 5) and describe some auxiliary science opportunities in Section 6. We describe our survey strategy in Section 7 and our software and calibration in Section 8, and conclude in Section 9. *This proposal is limited to 30 pages. We have written a much more detailed White Paper describing the project feasibility and technical details for various science cases; it is available at* `http://hscsurvey.pbworks.com/w/page/60427271/HSCWhitePaper`.

2 The HSC Instrument

While there are many 8-meter class telescopes around the world, Subaru is the one with by far the largest field of view. Suprime-Cam (Miyazaki et al. 2002a), with its $\sim 0.25\,\mathrm{deg}^2$ field of view and superb delivered image quality (routinely $0.7''$ FWHM), has been a world leader in wide-field studies of the distant and faint Universe. Hyper Suprime-Cam, its successor, takes advantage of the full accessible field of view of the Subaru telescope (1.5° diameter), and thus has a survey power about 7 times larger than that of Suprime-Cam.

The instrument has been designed and built by a team at NAOJ, led by Satoshi Miyazaki, the PI of this proposal, and was funded by the Grant-in-Aid for Scientific Research in Priority Areas "Exploring Dark Energy with Wide-field Imaging" and the FIRST program "Subaru Measurements of Images and Redshifts" (SuMIRe), CSTP, and WPI, MEXT, Japan, as well as Princeton University and ASIAA in Taiwan. The basic components of the instrument are described in Table 2.

The instrument has a large and optically very sophisticated seven-element Wide-Field Corrector (WFC), designed and built by Canon, which incorporates an Atmospheric Dispersion Corrector (ADC) and delivers a instrumental Point-Spread Function (PSF) with a diameter enclosing 80% of the light (D_{80}) of $0.2''$ or better over the entire field in all filters. A Prime Focus Unit (PFU) built by Mitsubishi, which incorporates a precise hexapod for attitude and focus adjustment, holds the WFC and the camera in place at the telescope prime focus. The entire structure is 3 meters tall, and weighs 3 tons. The corrector gives an unvignetted field of view to a diameter of 10 arcmin; vignetting is a roughly linear function of field radius, reaching 26% at the edge of the field at 0.75°. The Subaru top-end structure has been modified to accommodate the PFU and WFC. The WFC can be used by other wide-field instruments as well, and is incorporated into the design of the planned Prime Focus Spectrograph.

The focal plane is paved with a total of 116 Hamamatsu Deep Depletion CCDs, each $2\,\mathrm{K} \times 4\mathrm{K}$. Four of

Table 2: **Hyper Suprime-Cam Characteristics**

Instrument weight	3.2 tons (estimate)
Field of View	1.5° diameter, 1.77 $\deg^2$
Vignetting	0 at 0.15°; 26% at edge
Pixel scale	15μm = $0.16''$
Delivered Image Quality	$D_{80} < 0.2''$ in all filters
CCDs	116 2K × 4K Hamamatsu Fully-Depleted
CCD QE	40% at 4000Å, 10,000Å; 95% at peak (at -100°C)
CTE	0.999999
Readnoise	4.5 e^-
Data Rate	2.31 GBytes/exposure (16-bit A-to-D)
Focal ratio at Focal Plane	2.25
Overhead between Exposures	29 sec
Wide-Field Corrector	7 optical elements, ADC
Shutter	Roll-Type
Filters	*grizy* + 4 NB; Table 8
Filter Exchanger	6 filters installed at a time
Filter Exchange Time	10 minutes

these are used for guiding and eight for automatically monitoring focus, leaving 104 science detectors with a total area of 1.77 $\deg^2$. These chips, which are three-side buttable and each have four independent readout amplifiers, are currently installed in Suprime-Cam, which has demonstrated their excellent characteristics: low read noise, excellent charge transfer efficiency, few cosmetic defects, and most importantly, high quantum efficiency from 4000Å to 10,000Å (blueward of 4000Å, the response is limited both by the CCDs and the optical elements in the WFC). The model system response, including reflectivity and transmission of all optics, is shown in the right panel of Figure 1. The CCD pixels are 15μm on a side, corresponding to $0.16''$ at the focal plane. At this resolution, the images will be well-sampled in even the best seeing. Ray-tracing of the optics has shown that ghosting is minimal, with the worst ghost at an illuminance (fractional light in a PSF aperture) of $\sim 5 \times 10^{-8}$.

The instrument is installed at prime focus using the existing Top Unit Exchanger (TUE) instrument handler, though modifications were necessary to ensure that the delicate ceramic housing of the corrector lens is not damaged during installation, as clearances are very small.

The camera has a roll-type shutter, with excellent timing accuracy, allowing uniform exposure time over the field of view. Including readout and all overheads, the minimum time between exposures is 29 seconds, allowing for efficient surveying of the sky. The filter exchange mechanism can hold six filters at one time, and requires about 10 minutes to exchange filters, with the telescope at zenith. The complement of filters can be changed during the daytime. As described in Section 7, our survey will use five broad-band filters (*grizy*) modeled on the SDSS filter set (the right panel of Figure 1), as well as four narrow-band filters to observe Lyα at a wide variety of redshifts. All the broad-band filters and one of the narrow-band filters are in hand; the other three will be delivered in March 2013. HSC was put on the telescope for the first time in August 2012, which allowed us to confirm that the optics of the WFC give good images.

3 Cosmology Science

3.1 HSC cosmology objectives

Characterizing the properties of dark energy (DE) is one of the primary goals of the HSC survey. DE causes the expansion of the Universe to accelerate at late times, so it can naturally be probed by measuring the expansion rate as a function of redshift, $H(z)$ (the rate today $H(z=0) \equiv H_0$, the Hubble constant). DE also affects the growth rate of large-scale structure $G(k,z)$, leading to additional observables to constrain its properties. The expansion rate has been constrained from observations of CMB, type-Ia supernovae (hereafter SNeIa), and Baryon Acoustic Oscillations (BAO), and the HSC survey will improve the constraints with observations of high-redshift SNeIa at $z > 1$. The growth rate of large-scale structure will be measured to unprecedented precision from weak lensing. Combining these probes can not only measure the parameters of DE, but also test alternative models in which modifications to General Relativity cause the accelerated expansion of the Universe. We can also use HSC observables to probe the primordial power spectrum $P_\zeta(k)$ and primordial non-Gaussianity, both of which contain a wealth of information about early

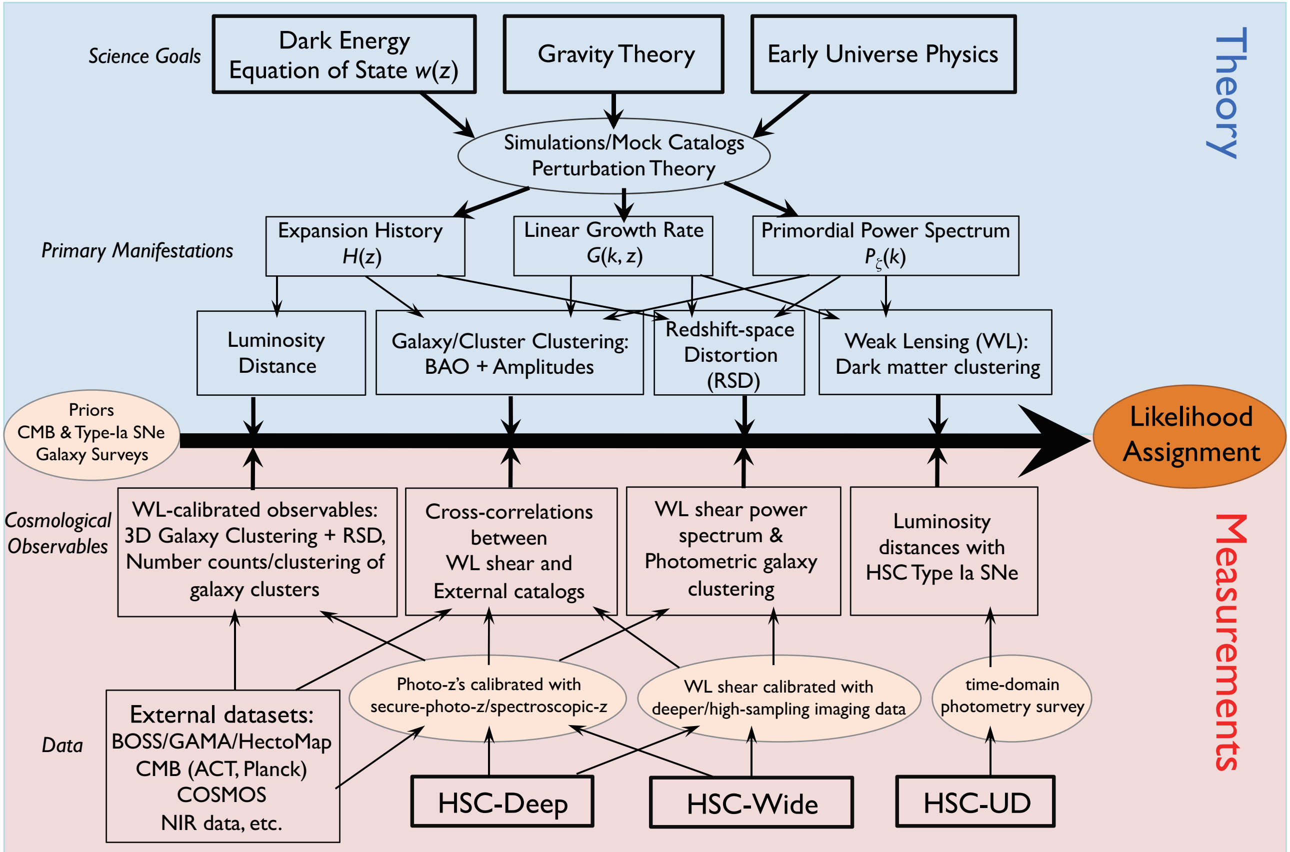

Figure 2: Work flow for HSC cosmology. Boxes are data or models; ovals hold tasks necessary to process them. Top-level science goals (top of the chart) set theory tasks required for developing accurate models of the observables. The imaging data and external data sets are at the bottom, and observables are indicated along the analysis path (arrows) we are planning to follow. The heavy arrow in the middle indicates that we will compare theory predictions to measurements to yield likelihood assignments for possible dark energy/modified gravity models.

Universe physics.

To probe these functions, we will use the following observables: (1) We will measure the *coherent distortion of galaxy shapes produced by WL*, in order to reconstruct the distribution of all matter (including dark matter) in foreground structures, and combine the weak lensing results with photometric redshift information to reconstruct the matter field as a function of angular position and redshift. (2) We will robustly constrain cosmology by *measuring the auto- and cross-correlations of the galaxy distribution and shear field*[2] *available from HSC and other data sets*, including the SDSS-III BOSS spectroscopic galaxies and secondary CMB effects (CMB lensing and the Sunyaev-Zel'dovich, or SZ effect) measured by the Atacama Cosmology Telescope (ACT) and Planck experiments. (3) We will identify *∼120 high-redshift SNeIa with well-sampled lightcurves* from the Ultradeep layer to measure the distance-redshift relation, which we will combine with CMB and the BAO measurements to tighten constraints on the expansion history.

Converting the HSC observables into cosmological constraints requires us to account for complications such as the non-linear evolution of the matter distribution and galaxy formation. We will use N-body simulations and mock catalogs to construct sufficiently accurate model predictions to compare with the high-precision measurements of HSC observables (Sato et al. 2009; Takahashi et al 2009, 2011; Shirasaki et al. 2012).

Figure 2 illustrates our working flow chart. The top half shows how we will develop predictions for the observables in terms of $H(z)$, $G(k, z)$ and $P_\zeta(k)$. The lower half shows how we will construct our primary observables with HSC data alone and in combination with other data sets. The figure makes clear that we need all three survey layers to construct our observables. By comparing the measurements with the

[2]Higher-order correlations carry additional cosmological information. Measuring them is therefore an enhanced goal for the HSC cosmology program (Takada & Jain 2004; Kayo et al. 2012).

theories, we will make likelihood assessments of possible DE/modified gravity theories. Our goal is to derive cosmological constraints from HSC at a precision comparable to a Dark Energy Task Force (DETF; Albrecht et al. 2006) Stage-III experiment. Then we will achieve constraints comparable to a Stage-IV experiment from a joint analysis of HSC, Planck, ACT, and BOSS, and eventually with the PFS survey. The areas and depths of the Wide, Deep, and Ultradeep layers are designed to meet these science goals.

3.2 Technical approach and methodology

HSC weak lensing cosmology: Weak lensing measurements are a powerful probe of cosmology because they directly trace the projected distribution of matter in the Universe. Our survey will find of order $n_{\rm eff} \sim 20$ galaxy/arcmin^2 (estimated from Suprime-Cam data with similar depths) for shape measurements, the highest-quality data available over the next decade before LSST and Euclid see first light. The high-quality measurements of shapes and photometric redshift (photo-z) from the *grizy* photometry will enable three-dimensional measurements of the shear-shear power spectrum and cross-correlations between the shear measurements and the large-scale distribution of galaxies and galaxy clusters.

Cosmic shear: Cosmic shear, the auto-correlation of galaxy shapes due to lensing by intervening large-scale structure, has long been considered one of the most promising ways to constrain structure growth and, therefore, DE (Takada & Jain 2004). The left panel of Figure 3 shows the expected cosmic shear power spectrum measurement for HSC-Wide. The total signal-to-noise ratio is $S/N \simeq 143$ when combining three redshift bins and angular scales up to maximum multipole $l_{\rm max} = 2000$, a factor of 5 improvement over the current best measurements (CFHTLenS; Heymans et al. 2012). Our cosmic shear measurements will have higher S/N than those for DES[3] ($S/N = 111$), and will cover a broader range of redshift. The right panel of Figure 3 shows how accurately the DE equation of state $w(z)$ can be constrained by cosmic shear tomography with three redshift bins, combined with the Planck CMB information. The expected DE constraints are $\sigma(w_{\rm pivot}) = 0.045$ and DE FoM$= 24$ for HSC[4], compared to $\sigma(w_{\rm pivot}) = 0.046$ and FoM$= 20$ for DES. Thus HSC and DES have a comparable cosmological power, and are complementary to each other in the sense that they probe different redshift ranges. These forecasts assume that systematic errors are well under control; we have a comprehensive program for constraining systematic errors in these weak lensing measurements, including a suite of consistency checks to be carried out on the data itself (including measurements using HSC-Wide and Deep layers) and external data (spectroscopic surveys, space-based imaging, and CMB data), as well as a planned set of tests using realistic image simulations – see below and Section 3.4 for more details.

Galaxy-galaxy lensing and galaxy clustering: Our WL cosmology program will also employ lensing cross-correlations with tracers of large-scale structure (galaxy-galaxy or cluster-galaxy lensing), a useful method to restore the redshift information of the WL field. Cross-correlating galaxy shapes with the positions of foreground objects that have spectroscopic or secure photo-z redshift estimates (e.g., BOSS galaxies or clusters) yields a measurement of the mean tangential shear γ_t as a function of separation, $\langle\gamma_t\rangle(r_\perp; z_l) \propto \langle\Delta\Sigma_{hm}(r_\perp; z_l)\rangle|_{r_\perp = d_A(z_l)\theta}$, where the factor of proportionality is related to the distances to the lens and source along the line-of-sight. Here, $d_A(z)$ is the angular diameter distance to redshift z; $r_\perp = d_A(z_l)\theta$ is the projected radius from the foreground tracers; and $\langle\Delta\Sigma_{hm}\rangle(r_\perp; z_l)$ is the mean excess mass profile around the tracers at z_l. While the total lensing effect on distant galaxies comes from all foreground structures projected over Gpc scales in the radial direction, the cross-correlation is sensitive to the lensing contribution by lenses at a particular redshift z_l, thereby enabling a *tomographic reconstruction* of the lensing structures as a function of redshift and of physical separation. It has been shown (Baldauf et al. 2010; Mandelbaum et al. 2012) that combining this measurement of the galaxy-mass correlation with the galaxy clustering enables a relatively model-independent measurement of the growth of structure in the matter density field, while simultaneously constraining the relationship between the galaxy and matter density fields on large scales. Because cosmic shear is a shear auto-correlation and galaxy-galaxy lensing is a shear cross-correlation, the two measurements are affected differently by systematic errors (Mandelbaum et al. 2005), thus comparing the two can give us confidence that these systematics are under control. The galaxy-galaxy lensing and cluster-galaxy lensing signature can be measured over relatively small solid angles, making this approach particularly valuable for constraining cosmological parameters with the first year or two of HSC survey data.

[3]For DES, we assume a mean source redshift $\langle z_s\rangle = 0.7$, effective number density $\bar{n}_{\rm eff} = 10$ arcmin^{-2}, and area of 5000 deg^2.

[4]The DE figure-of-merit (DE FoM) is defined as DE FoM $\equiv [\sigma(w_{\rm pivot})\sigma(w_a)]^{-1}$, where $\sigma(w_{\rm pivot})$ is the best-constraint error on w_0 at the pivot redshift and the errors include marginalization over other parameters.

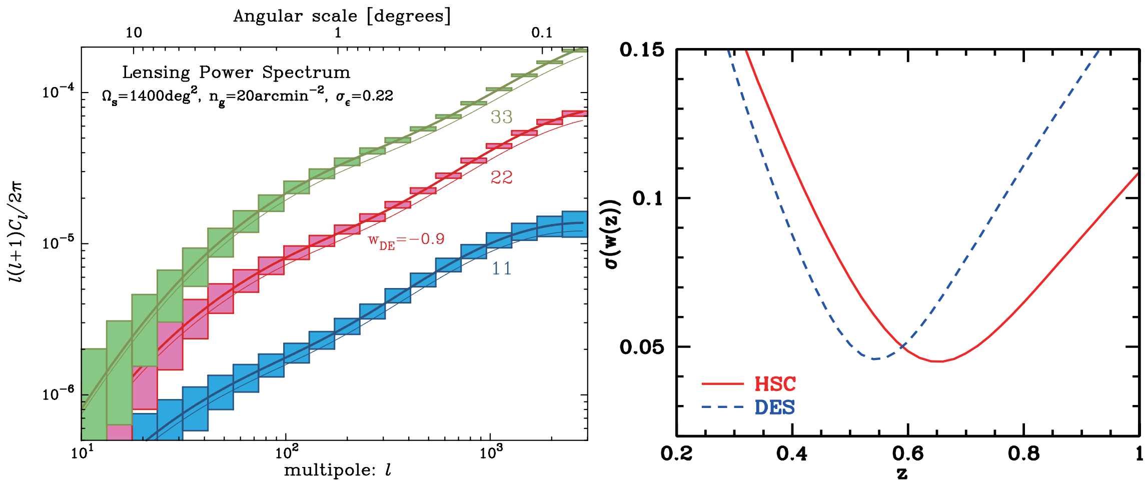

Figure 3: *Left*: Expected weak lensing cosmic shear power spectra for three redshift bin tomography, where boxes around each curve show the expected 1σ measurement accuracies. Thin curves are computed using a model in which the DE equation of state is changed to $w_{\rm DE} = -0.9$ from $w_{\rm DE} = -1$, demonstrating that we will be able to cleanly distinguish between these two models. *Right*: The marginalized error on $w(z)$ as a function of z, expected from cosmic shear tomography assuming three redshift bins and using the power spectrum information up to $l_{\rm max} = 2000$ for the HSC and DES surveys combined with data from Planck. Here we employ the standard parametrization $w(z) = w_0 + w_a[z/(1+z)]$ to model the DE equation of state.

Combining weak lensing with the halo mass function: We will also use the method proposed in Oguri & Takada (2011) to constrain cosmology with minimal systematic errors, by measuring cluster-galaxy lensing using a *single* population of background source galaxies, for distinct lens redshift slices up to $z_l \lesssim 1.4$. Since the source redshift (z_s) dependence of the cross-correlations appears only via a geometrical factor $\langle d_A(z_l,z_s)/d_A(z_s)\rangle_{z_s}$, the relative strength of cross-correlation signals for different z_l allows us to calibrate out source redshift uncertainty (see Oguri & Takada 2011 for details), thereby relaxing the photo-z error requirements for the cluster-galaxy lensing. Then we can combine the cluster-shear cross-correlation with the cluster auto-correlation function and the number counts of clusters, which are highly sensitive to the amplitude of matter fluctuations and the DE equation of state. While the traditional cluster count approach is subject to uncertainty in the mass-observable relation, Oguri & Takada (2011) showed that combining measurements of the stacked WL and the cluster auto-correlation function directly constrains the mass-observable relation, and thus breaks its degeneracy with cosmological parameters. This approach is attractive because the rich data sets (especially BOSS and ACT) in the HSC footprint allow us to construct a robust, complete sample of clusters (see below). We will demonstrate in Section 3.3 that the cluster-shear cross-correlations can constrain cosmological parameters to a precision similar to that of the more standard cosmic shear tomography with optimistic assumptions on systematic errors, even after accounting for and fully marginalizing over these systematic errors.

The left panel of Figure 4 shows the expected, cumulative S/N for the WL cross-correlation, i.e., stacked WL signals due to clusters with masses $M_{\rm halo} > 10^{14}h^{-1}M_\odot$ in redshift slices of $\Delta z = 0.1$ as a function of the lens redshift, computed using the method described in Oguri & Takada (2011). The two curves are the results expected for the proposed HSC Wide-layer and for DES. The figure shows that HSC measures the stacked WL signals for halos at higher redshift than DES, given its greater depth. HSC WL allows a significant detection of lensing by large-scale structure around clusters out to $z \sim 1$; this signal arises from the average mass distribution surrounding the lens halos and is easier to model theoretically, as mentioned above.

Overall approach: We will maximize the cosmological information in our analyses by combining multiple observations, including cosmic shear, the galaxy- and cluster-galaxy lensing, and the galaxy/cluster auto-correlation. The ability to constrain structure growth and therefore cosmological parameters (Figure 2) in several ways is especially valuable given the systematic uncertainties due to shape measurement, photo-z error, and intrinsic alignments of galaxy shapes due to tidal fields (which mimic WL signals). We find that combining these different measurements, while marginalizing over systematics, restores the loss of information in cosmic shear alone from those systematics (Joachimi & Bridle 2010). We also plan to measure lensing magnification (e.g., Huff & Graves 2011) of galaxy sizes and fluxes, which probes the line-of-sight matter density with different observational uncertainties, providing an additional cross-check and further improving on shear-based cosmological constraints.

Synergy with other cosmological data sets: The HSC survey footprint overlaps other data sets, such as the SDSS and the ACT survey. While the HSC survey alone can constrain the DE equation of state parameter to a precision comparable to a DETF Stage-III experiment, $\sigma(w_{\rm pivot}) \simeq 0.04$ (see Section 3.3), and this constraining power is the primary motivation for our survey, we also note several synergistic science cases with overlapping data sets.

The SDSS-III BOSS survey (Dawson et al. 2012) is a spectroscopic survey of massive galaxies with $0.3 \lesssim z \lesssim 0.7$ targeted from the SDSS imaging. These luminous red galaxies (LRGs) preferentially reside in massive dark matter halos, $M_{\rm halo} \gtrsim 10^{13} M_\odot$ (White et al. 2011). However, the WL effect due to these halos is measured only at low S/N due to the shallowness of the SDSS imaging. The HSC survey goes roughly 4 magnitudes deeper, increasing the total lensing S/N (for 0.1–60 h^{-1}Mpc) from ~ 15 to ~ 200. Figure 4 (middle panel) shows the expected total WL S/N around the BOSS galaxies using HSC sources, as compared with existing SDSS WL measurements.

A major uncertainty for the BOSS experiment is the unknown relationship between the galaxy and dark matter distributions, including the nonlinear galaxy bias, redshift-space distortions (RSD), and the Finger-of-God effect due to virial motions of galaxies within their dark matter halos (Hikage et al. 2012). Since the HSC survey region covers a representative subset of the BOSS survey region (about 15%), the HSC WL can calibrate these systematic uncertainties. For instance, simulations suggest that we can combine the BOSS galaxy power spectrum with BOSS galaxy-galaxy lensing in HSC to directly measure the scale-dependent bias of BOSS galaxies, $b(k) \propto (P_{\rm BOSS}(k)/P_{\rm BOSS-\gamma}(k))^{1/2}$, to a few percent accuracy at each k-bin up to $k \simeq 0.2\ h{\rm Mpc}^{-1}$, for $0.1 \le z \le 0.7$ with bin width $\Delta z = 0.1$ (Nishizawa et al. *in prep.*). This bias reconstruction will enable us to use the amplitude and shape of the BOSS galaxy redshift-space auto-correlations, both to constrain cosmology and to extract the RSD from anisotropic modulations of the redshift-space power spectrum. By combining the RSD with dark matter clustering from WL, we can perform a model-independent test of gravity on cosmological scales, because the peculiar velocity field is related to the dark matter distribution via gravity theory (Reyes et al. 2010; Guzik et al. 2010: Tang et al. 2011).

In Reyes et al. (2010), spectroscopic and imaging data from the SDSS were used to measure a parameter called E_G, which is insensitive to the amplitude of matter clustering and galaxy bias, and constrains a combination of the growth rate and the ratio of the metric potentials (each of which could in principle be modified in alternative gravity theories). This measurement requires overlapping spectroscopic and imaging data, and we estimate that the combination of HSC imaging with BOSS spectroscopy will allow E_G to be constrained to the 4% level, with roughly equal error budgets coming from the RSD and the lensing measurements. Unlike the 16% measurement with SDSS alone, this constraint will be enough to meaningfully distinguish between General Relativity and interesting models for modified gravity.

The cluster-shear cross-correlation technique relies on a robust catalog of galaxy clusters. We can construct a unique catalog of clusters by finding, around each SDSS or BOSS LRG[5], red member galaxies from the deep HSC images up to $z \simeq 0.7$ and further by adding higher-redshift clusters from the ACT SZ survey (see below). In addition, one of our Wide target fields overlaps the HectoMAP survey, a magnitude-limited spectroscopic survey for galaxies at $r < 21.3$ covering 55 deg^2 with the 300-fiber Hectospec instrument on the 6.5m MMT telescope, which provides a sample of about 300 optically-selected clusters with masses $M_{\rm halo} \gtrsim 10^{14} h^{-1} M_\odot$ and at $z \lesssim 0.6$, each with more than a few tens of member galaxies with spectroscopic redshifts (Kurtz et al. 2012). We will combine dynamical mass estimates from the line-of-sight velocity dispersion of member galaxies with HSC WL mass estimates to establish a well-calibrated mass-observable relation for the HectoMAP clusters, and to understand projection effects for our optically selected cluster sample. We can also find clusters as high peaks in the weak lensing mass map (Miyazaki et al. 2002b, 2007), which we will compare with the optically-selected clusters to test their robustness.

Combining the HSC survey and the arcminute-resolution, high-sensitivity ACT CMB experiment also offers unique, synergistic science opportunities. We are involved in the ACT experiment and its successor, ACTPol, and our Wide survey fields overlap almost completely with the ACTPol region. The ACT

[5]Massive halos with $\gtrsim 10^{14} h^{-1} M_\odot$ at $z \le 0.6$ typically host one or more SDSS/BOSS spectroscopic red galaxies (White et al. 2011).

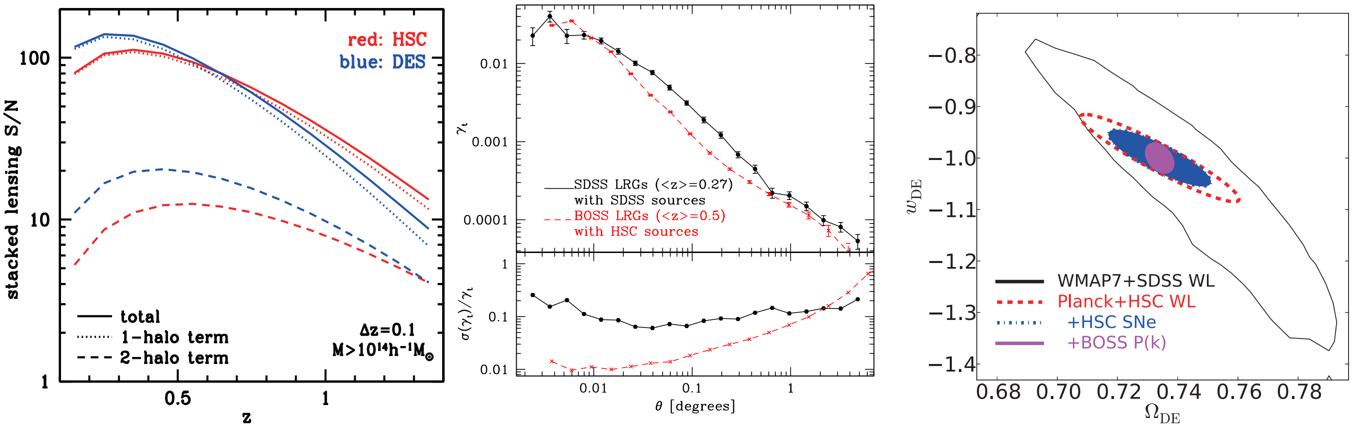

Figure 4: *Left*: The predicted cumulative signal-to-noise (S/N) ratios for the stacked WL signals due to halos with masses $M_{\rm halo} \geq 10^{14}h^{-1}M_\odot$ in redshift slices of $\Delta z = 0.1$, as a function of the lens redshift. The red and blue curves are the results for the HSC and DES surveys, respectively. *Middle:* The measured WL shear (solid black line) around SDSS LRGs covering 7131 deg^2 at $\langle z \rangle = 0.27$, using SDSS galaxies as sources (Mandelbaum et al. 2012), and the predicted shear and errors around BOSS galaxies at $\langle z \rangle = 0.5$ (dashed red line), from 1400 deg^2 of mock catalogs populated by galaxies to match the observed BOSS clustering signal (White et al. 2011), using WL measurements of background sources in the HSC survey. The bottom panel shows the inverse S/N per bin; the total S/N is ~ 30 for SDSS and ~ 200 for HSC. *Right*: The 68% C.L. constraint region for $\Omega_{\rm DE}$ and $w_{\rm DE}$ for several experiments, assuming flat wCDM (constant $w_{\rm DE}$). The outer black contour shows current constraints from WMAP7 and SDSS WL measurements (Mandelbaum et al. 2012). The smaller contours show the expected constraints for HSC, in combination with the expected Planck CMB constraints and/or the BOSS galaxy clustering.

experiment will provide a unique, redshift-independent catalog of SZ-selected clusters with nearly 100% completeness for very massive clusters ($> 8 \times 10^{14}M_\odot$) at all redshifts, especially those $z \gtrsim 0.6$ (Niemack et al. 2010). The upgraded ACTPol survey will identify clusters down to a smaller mass threshold, by a factor of a few, providing an opportunity to construct a large, clean sample of high-z clusters in the HSC footprint. As implied by the left panel of Figure 4, the HSC survey for WL studies of high-redshift clusters is quite synergistic with the ACT SZ survey.

Lensing of the CMB by large-scale structure can be cross-correlated directly with our cosmic shear maps. The CMB lensing and HSC-galaxy lensing signals at any given point on the sky arise from the same large-scale structure in the overlapping redshift range (which is large, given the depth of the HSC survey), and thus this cross-correlation measures the same signal as the cosmic shear power spectrum, with different systematics. We estimate that the statistical errors on the HSC shear-CMB lensing cross-power spectrum will be only 1.5 times as large as those on the cosmic shear power spectrum from HSC alone (and even better than that on the largest scales), suggesting that the cross-correlation with CMB lensing will add significant power to HSC.

Geometrical test with HSC SNeIa survey: The Ultradeep layer, with its carefully-chosen cadence for broad-band filter imaging, allows us to identify ~ 120 SNeIa with well-sampled lightcurves (Figure 12), 40 of which will be at $1 \lesssim z \lesssim 1.4$. The efficient detection of such high-redshift SNeIa is possible due to the unique capabilities of Subaru/HSC, its large aperture, field of view, and red-sensitive CCDs (y-band filter). The HSC SNeIa sample will be complementary to the current SNeIa sample (Suzuki et al. 2012), the majority of which are at $z \lesssim 0.7$, and to samples that will be delivered from multi-color imaging surveys with 4-m telescopes such as the DES SNeIa survey (Bernstein et al. 2012). In general, using these SNeIa for cosmology requires spectroscopic follow-up observations with 8-m class telescopes. However, type classifications and redshifts for many SNeIa will be available from multicolor lightcurve fitting and from photometric redshifts and spectroscopy of their host galaxies. Real-time spectroscopy of the supernova themselves is required for only ~ 20 SNeIa per year for which, e.g., no host galaxy is evident, and will be readily accessible given the breadth of our collaboration network.

3.3 Target accuracies of parameter constraints

We will derive stringent constraints on cosmological parameters following the methodology in Figure 2. Table 3 shows the expected accuracies of cosmological parameters based on the cluster-shear cross-correlation

Data	$w_{\rm pivot}$	w_a	FoM	γ_g	$m_{\nu,{\rm tot}}$[eV]	$f_{\rm NL}$	n_s	α_s
BOSS-BAO	0.064	1.04	15	–	–	–	0.018	0.0057
HSC(WL)-B (baseline)	0.080	0.86	15	0.15	0.16	30	0.014	0.0041
HSC(WL)-O (optimistic)	0.068	0.66	22	0.083	0.082	18	0.013	0.0040
HSC(WL+SN)-B	0.043	0.60	39	0.15	0.16	30	0.014	0.0041
HSC(WL+SN)-O	0.041	0.45	54	0.081	0.081	18	0.013	0.0040
HSC-O+[BOSS-$P(k)$]	0.028	0.36	99	0.038	0.076	17	0.011	0.0029
HSC-O+[BOSS+PFS]	0.027	0.19	196	0.035	0.07	17	0.009	0.0022

Table 3: Expected parameter accuracies for HSC cosmology using the Oguri & Takada (2011) shear method: The "Baseline" case ("HSC(WL)-B") uses clusters with $z < 1$ and masses $M_{\rm halo} > 10^{14}h^{-1}M_\odot$, and without priors on nuisance parameters, whereas the "Optimistic" case ("HSC(WL)-O"), uses clusters to $z = 1.4$, with some *conservative* priors on nuisance parameters. The DE constraints listed in this table are also conservative in the sense that the errors include marginalization over non-standard cosmological parameters such as γ_g, $m_{\nu,{\rm tot}}$, and $f_{\rm NL}$. The rows denoted "WL+SN" include the above HSC-WL and SNeIa measurements. The last two rows show the expected constraints when we combine the HSC observables with spectroscopic surveys, BOSS and PFS (see Ellis et al. 2012 regarding the planned PFS survey). The joint constraints assume that the HSC-WL observables can remove the spectroscopic galaxy bias uncertainty, by comparing the galaxy clustering with the dark matter distributions reconstructed from the HSC-WL observables. This analysis does *not* include constraints from cosmic shear, which is largely independent, with different systematics, and serves as a valuable cross-check.

approach, estimated using the Fisher information matrix formalism. For the parameter forecasts, we employed a conservative approach. In particular, we included both a broad range of cosmological parameters and a number of nuisance parameters to model systematic errors in the observables (such as photo-z errors and shear multiplicative error; see Oguri & Takada 2011). For SNeIa, we forecast constraints from 120 SNeIa discovered by the Ultradeep layer plus 150 local SNeIa at $z \sim 0.1$. We did not explicitly include systematic errors for the SNeIa Fisher matrix, but instead assumed a conservative error on the distance modulus of $\sigma(\mu) = 0.3$ per object. To quantify the power of the HSC survey for constraining the structure growth rate, we use the parameter γ_g, which is defined so that the linear growth rate is $G(z) \propto a\exp[\int_0^a {\rm d}\ln a' \, \{\Omega_{\rm m}(a')^{\gamma_g} - 1\}]$. Given sufficiently high accuracies for measuring w_0, w_a and γ_g, the HSC survey can constrain both the expansion history and the growth of large-scale structure. We also included other interesting parameters: the sum of neutrino masses $m_{\nu,{\rm tot}}$, the primordial non-Gaussianity parameter $f_{\rm NL}$, and the primordial power spectrum shape (the tilt n_s and the running index α_s).

Table 3 suggests that HSC WL observables alone can constrain DE parameters to high precision, similar to the Stage-III BOSS BAO experiment. The HSC DE constraints can be further improved when combined with the geometric constraints derived from the high-redshift SNeIa of the Ultradeep layer. Most importantly, because WL directly probes the clustering amplitude of dark matter as a function of redshift, the HSC WL observables allow us to make a stringent test of gravity on cosmology scales (via the parameter γ_g), when combined with the geometrical probes (BOSS BAO and the HSC- and external SNeIa). Furthermore, because the HSC survey fields lie completely within the BOSS survey footprints, we will combine the HSC WL measurement with the BOSS clustering measurement to directly calibrate the galaxy bias. The combination will allow us to significantly improve the cosmological constraints, achieving $\sigma(w_{\rm pivot}) \simeq 0.03$ and FoM$\simeq$ 100. Figure 4 shows the improvement on cosmological parameter constraints that this analysis will yield. The constraints we will get from cosmic shear (Figure 3) are largely independent (and with different systematics), and will act as a valuable cross-check of our results, and allow even tighter constraints on parameters.

3.4 Observational challenges

To achieve the cosmological constraints above, we must control various systematic errors in these cosmological observations. We discuss here the two most important such effects: the measurements of galaxy shapes for WL, and photometric redshifts.

Shape measurements: The HSC data processing pipeline (Section 8.1) will make accurate measurements of PSF and galaxy shapes needed for WL cosmology. Several methods use second moments of the surface brightness to estimate the galaxy ellipticity: KSB (Kaiser, Squires & Broadhurst 1995; Miyazaki et al. 2002b; Okabe et al. 2010; Oguri et al. 2012), an extended KSB method using elliptical weight functions, E-HOLICs (Okura & Futamase 2012), the re-Gaussianization method (Hirata & Seljak 2003; Mandelbaum et al. 2005) and a Fourier-domain method (Zhang 2008; Katayama et al. *in prep.*). Others are model-dependent methods, where the galaxy ellipticity is estimated by fitting the measured image to the model galaxy profile convolved with the PSF: a shapelet method (Bernstein & Jarvis 2002; Miyatake et al. 2012), multi-scale shapelets (Bosch 2010), and the Spergel method (Spergel 2010; Hikage et al. *in prep*). We are testing all these methods using simulated images generated from COSMOS *Hubble Space Telescope (HST)* data (Mandelbaum et al. 2011) and Suprime-Cam data on galaxy clusters to quantify the performance of each method (Hikage et al. *in prep*; Miyatake et al. 2012; Reyes et al. 2012). We will use these different methods to make various cross-checks of accuracies and systematic errors in the estimated galaxy ellipticities, and will also use simulation software from the upcoming lensing community data challenge (co-led by R. Mandelbaum), modified to include real HSC optics and detector effects, to test for errors due to *all* stages of the data analysis. From the simulation studies thus far, we have found that several of these methods achieve an accuracy better than a few percent ($\lesssim 1\%$ for the best method, even for $S/N \sim 20$ galaxies with realistic galaxy morphologies) for the shear multiplicative error, which shows we are on our way to achieving the goals in Section 8.1.

We have designed the HSC survey strategy (Section 7.3) to better control WL systematic errors. Individual exposures are ~ 3 minutes long, and thus we will have 6-7 exposures for each i-band pointing. First, we will take the i-band imaging data when the seeing is sufficiently good ($0.40'' <$ FWHM $< 0.7''$, where the lower threshold helps avoid the undersampling of PSF images). Second, we will employ a large-angle dithering strategy so that objects appear in different positions of the focal plane in each exposure, thus (at least partially) canceling out the different optical and detector effects over the multiple exposures. Third, we spread the exposures of a given field over different nights, giving independent sampling of the atmospheric PSF.

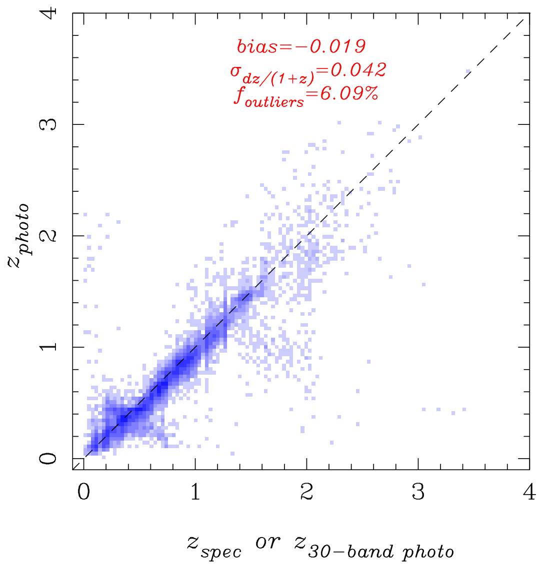

Figure 5: The scatter between true and photo-z estimated redshifts for simulations of the HSC-Wide layer. This simulation extends to $i = 25$, and uses redshifts from the zCOSMOS and 30-band photo-z COSMOS catalogs (Lilly et al. 2009; Ilbert et al. 2009). We used the photo-z posterior distribution of each galaxy to clip photo-z outliers.

We use the Deep layer data to calibrate various aspects of our WL measurements. The higher S/N of the Deep exposures allows us to carry out a statistical study of galaxy properties (disk/bulge components, and the intrinsic ellipticity distribution) over a cosmologically fair volume. A better understanding of the intrinsic galaxy population is necessary in order to interpret lensing shape measurements, In addition, the many exposures in the Deep layer will provide a full database of different observing conditions for each star and galaxy: position in the focal plane, seeing, elevation, and so on. Thus, we can use the Deep data to study how observing conditions propagate into errors in galaxy shape measurements. We will also use the Deep data to better understand noise rectification bias (the bias in lensing shear due to noise in the galaxy images, which occurs because shape measurement is a non-linear operation; Mandelbaum et al. 2011) by exploring shape measurements as a function of S/N. Thus, while the Deep layer does not cover enough solid angle for a cosmological lensing analysis on its own, it is critical for calibrating systematic errors in the Wide layer.

Photometric redshifts: The uncertainty in photo-z estimates is another potential major source of systematic error in WL analyses. To quantify this, we have constructed a mock HSC galaxy catalog based on COSMOS photometry (Capak et al. 2007), with simulated magnitudes and errors as they would be observed given the HSC depths and filters. By running various commonly used photo-z codes and our own custom code, we have estimated that our expected scatter and outlier fractions in the Wide layer will be $\sigma_{dz/(1+z)} = 0.082$, $f_{\rm outlier} = 13\%$ for galaxies down to $i = 25$.

Our HSC fields overlap a significant number of public spectroscopic surveys, including SDSS/BOSS, zCOSMOS, GAMA, HectoMAP, DEEP2/3, PRIMUS, VIPERS, and VVDS (see Section 7.2), which we will use to calibrate our photo-z templates and techniques at the bright end (to $i \sim 23$). We will extend the calibration ladder to fainter magnitudes using the deep, multi-wavelength photometry available in the Deep and Ultradeep layers. The photo-z's based on these exquisite data are much more accurate, with a scatter of order 0.04, than those for the Wide layer and can be used to calibrate and understand the photo-z's for Wide.

Another strength of HSC for photo-z's is its superb photometric calibration (1%), as detailed in Section 8.2. Our galaxy model-fitting code will allow us to estimate galaxy colors using only the bulge component, which has an older stellar population and a more reliable photo-z estimate. We will use the multiple repeat exposures in the Deep and Ultradeep layers to demonstrate the robustness of the galaxy colors, and thus photo-z's, as a function of observing conditions.

Among the various WL techniques that we will use for HSC, shear tomography has the most stringent constraints on photo-z's (Hearin et al. 2010). We carried out simulations using the mock HSC photo-z catalog described above, together with mock HSC lensing data based on COSMOS WL catalogs (Leauthaud et al. 2007). If we use information from the Deep layer on the redshift distribution, or remove likely photo-z outliers based on the photo-z posterior probability distribution (Nishizawa et al. 2010), the systematic errors on $w_{\rm pivot}$ and w_a from photo-z errors become comparable to our statistical errors. Figure 5 demonstrates accurate photo-z's with the outlier clipping applied; here the rms scatter in $z/(1+z)$ is 0.042, with an outlier fraction of 6%. We will reduce these systematic errors further by using the cross-correlation method (Newman 2008) with spectroscopic data from BOSS.

4 The Evolution of Galaxies at Intermediate Redshift

4.1 Overview: The unique power of the HSC Survey

The HSC survey will enable significant advances in the study of galaxy evolution at $z < 2$ because of its unprecedented sample size and statistical precision, high quality WL measurements, and superior spatial resolution.

Table 4 summarizes the HSC galaxy sample in photometric redshift bins[6] from the Wide and Deep layers, incorporating 20 million and half a million galaxies, respectively. These enormous samples allow us to study the properties in fine bins of redshift, stellar mass, morphology, color, and star formation rate. The volumes covered in each of many redshift slices are comparable to that of the SDSS Main Galaxy sample (Strauss et al. 2002) which has been used to characterize the nature of galaxies at the present day. Thus cosmic variance, which has plagued galaxy evolution studies at high redshift, will be negligible in most contexts.

The Wide and Deep imaging depths are well-suited to galaxy studies at $z < 2$. Simulations of Wide layer stellar mass estimates normalized to the y-band show uncertainties of $\sim$0.2 dex and no systematic biases to $z = 1.1$ as compared to COSMOS masses normalized in the K-band. Extant K-band imaging in the Deep fields will provide reliable mass estimates to $z \sim 2$. Star formation rate estimates in HSC will be derived from spectral energy distribution (SED) fitting (e.g., Salim et al. 2009). Mostek et al. (2012) developed a star formation rate (SFR) estimator based on M_B, $(U - B)$, and $(B - V)$, which shows a scatter relative to that derived from L[O II] of 0.3 dex with no systematic biases, using imaging data more than a magnitude *shallower* than HSC-Wide.

As described in Section 3 and shown in Figure 4, galaxy-galaxy lensing allows us to measure halo masses for binned ensembles of the galaxy population. In this way, evolving subpopulations can be tied directly to their dark matter halos, providing immediate comparisons to models based on N-body simulations and testing proposed drivers of evolution, many of which ultimately depend on total mass.

The median expected seeing of $0.65''$ corresponds to a PSF whose area is 50% the size of a typical galaxy at $z \sim 1$ (see Table 4). This allows for size, concentration, and inclination measurements. In addition, 10–15% of HSC data will have a seeing FWHM of $0.35''$ or better, vastly increasing the volume and sample size of studies tracking detailed morphological evolution (e.g., bulge growth, bars, spiral arms).

4.2 The physics of growth, star formation quenching, and mass assembly at $z < 2$

Numerous studies have now confirmed that the SFR density in the Universe peaks roughly at $z \sim 1$–2 and then falls by a factor of $\sim$30 to the present day (e.g., Hopkins et al. 2006a). The average amount of star formation depends on the stellar mass, M_*; low-mass galaxies typically form stars at a greater relative rate, and their star formation is quenched later, than in high-mass galaxies. The processes responsible for these phenomena are poorly understood, but operate against the backdrop of continuing mass assembly

[6]These are accurate enough to resolve timescales of $\sim$ 1 Gyr, typical for a variety of evolutionary processes.

		HSC-Wide			HSC-Deep		
z	$0.65''$ (kpc)	Vol (Gpc^3)	$\log M_*^{\rm lim}$	$N_{\rm gal}$	Vol (Gpc^3)	$\log M_*^{\rm lim}$	$N_{\rm gal}$
0.1	1.2	0.1	8.2	0.4M	0.001	8.7	7.2k
0.3	2.9	0.5	8.9	2.2M	0.008	9.3	38.3k
0.5	4.0	1.0	9.4	4.4M	0.019	9.8	71.8k
0.7	4.6	1.6	9.8	6.0M	0.029	10.1	94.4k
0.9	5.1	2.6	10.0	8.8M	0.049	10.2	137.3k
1.2	5.4	3.9	11.5	0.1M	0.073	10.4	166.2k
1.5	5.5	4.5	11.6	23k	0.083	10.6	145.7k
1.8	5.5	4.8	11.8	1k	0.090	10.8	108.9k

Table 4: Galaxy sample characteristics in a series of redshift slices for both Wide and Deep. The first column provides the mean redshift of each slice. The second column gives the physical scale subtended by $0.65''$, the median i-band seeing in both layers. The remaining columns indicate the volumes, stellar mass completeness limits, and number of galaxies expected above these limits for both layers. For Wide at $z < 1$, $\log M_*^{\rm lim}$ is defined by the faintest *red* galaxy that is detectable with a y-band flux 1 mag shallower than our 5σ depth limit. At $z > 1$, we switch to a UKIDSS/LAS K-band 5σ depth limit of $K = 20.2$ AB. For Deep, mass limits correspond to 1 mag shallower than a 5σ limit of $K = 22.8$ AB. We assume a standard cosmology with $H_0 = 70$ km s^{-1} Mpc^{-1}.

driven by galaxy interactions and mergers, as well as gas infall from larger scales. By precisely charting the star formation rates and stellar masses—and tying these to the halo masses ($M_{\rm halo}$)—for an unprecedented sample of galaxies, the *HSC survey will constrain the physical mechanisms that regulate star formation and develop the first complete picture of how galaxy mass is formed and assembled since $z \sim 1$.*

1) How do star formation and mergers drive mass assembly? Most previous studies of the crucial $1 < z < 2$ regime, such as GOODS, have surveyed tiny regions of sky, $\sim$0.1 deg^2. The Deep layer will be more than 200 times larger, enabling a comparison between star formation and stellar mass growth at the epoch when the global SFR begins to decline.

At $z < 1$, the Wide layer will provide the statistical power necessary to compare mass growth from new stars to that assembled via mergers. The two panels in Figure 6 show how HSC will be able to measure evolution in the star formation rate and the stellar mass function, respectively. Meanwhile, merger rates in HSC will be derived both from morphological irregularities (calibrated with comparisons to high-resolution merger simulations; Lotz et al. 2011) and pair counting with photo-z contamination corrections (e.g., Kartaltepe et al. 2007, but see also Lin et al. 2010). Because the HSC imaging is so deep, statistical studies of the merger rate down to very low mass ratios (e.g., 1:30), especially in the low-z regime, will be possible. These quantities are related via the M_* continuity equation: $\dot{N}(M_*, z) = {\rm SFR}(M_*, z) + {\rm Mergers}(M_*, z) - \dot{M}_{\rm loss}(M_*, z)$, where $\dot{N}(M_*, z)$ represents the evolving stellar mass function, ${\rm SFR}(M_*, z)$ includes fresh gas infall, and $\dot{M}_{\rm loss}$ accounts for mass loss due to stellar evolution as well as tidal stripping. By testing the validity of this equation, we can constrain $\dot{M}_{\rm loss}$ and identify inconsistencies that may reveal an evolving initial mass function (IMF) or changes in the merger timescale.

2) How is star formation fueled? Different fueling mechanisms such as cold flows, re-accretion of winds, cooling from a hot gaseous halo, and cold gas carried in by mergers lead to different timescales and degrees of stochasticity in the star formation history of galaxies. Mergers in particular should drive bursty modes of star formation (e.g., Cowie & Barger 2008) while gradual accretion or cooling produce smoothly varying modes (e.g., Noeske et al. 2007). HSC will provide definitive answers by delivering the statistical precision necessary to measure the SFR distribution in different M_* and redshift bins (left panel of Figure 6). In a given bin, the presence and strength of a tail towards high rates of star formation reveals the frequency of galaxies in a "burst" mode, e.g., those having a SFR greater than their M_* divided by the Hubble time.

3) What causes quenching? In addition to a global decline in the SFR, star formation in high mass galaxies at $z \sim 1$ is observed to shut down entirely; the mechanism driving this "quenching" remains unclear. At later times, quenching occurs in lower-mass galaxies (e.g., Bundy et al. 2006). Comparing the evolving SFR and mass functions in Figure 6 will determine the quenching rate, a key step in understanding whether quenching is violent (e.g., AGN feedback) or gradual (e.g., starvation).

Further insight will come from measuring "flow diagrams" of various galaxy populations (see Figure 7). For the first time, HSC will determine definitive evolutionary links by precisely equating the diminishing numbers of one population (e.g., star-forming galaxies) with the rising occurrence of another (e.g., quenched disks or ellipticals). The SFR versus bulge-to-total flow diagram in Figure 7 would reveal the relative

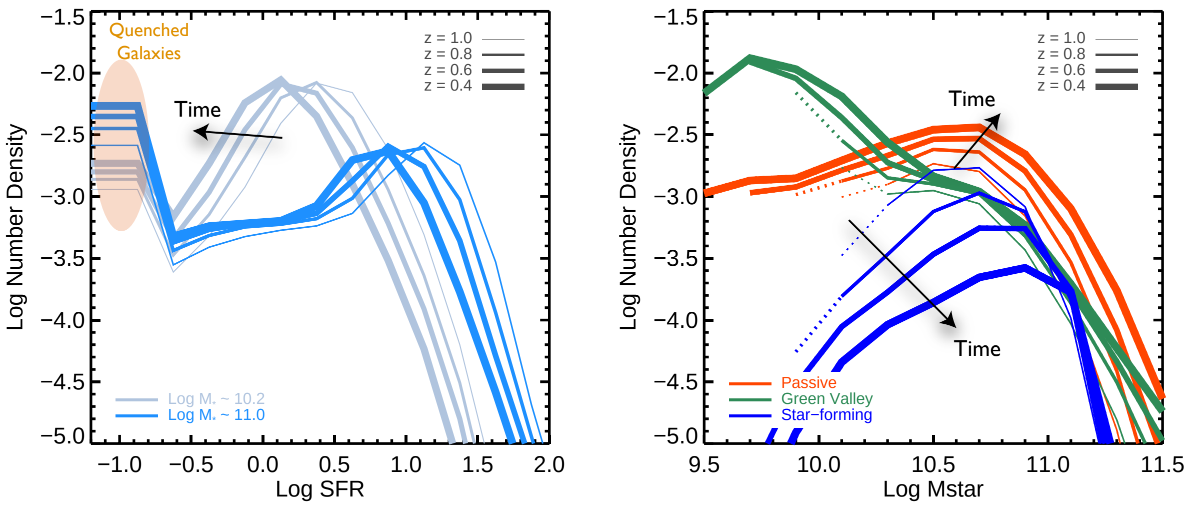

Figure 6: Expected HSC constraints on the galaxy number density evolution in the SFR-stellar mass plane, based on the Millennium Simulation (de Lucia et al. 2006). The left panel shows the number density as a function of SFR in two bins of stellar mass, while the right panel plots the same quantity as a function of mass in bins of SFR. In both cases, the line thickness increases with time. The dashed portions of the mass functions in the right-hand panel show the deeper mass completeness limits of the Deep layer. The plots demonstrate the statistical power of HSC observations to reveal modes of star formation at different masses and their contribution to the galaxy mass assembly history.

importance of two different quenching channels. In the present example drawn from the Millennium Simulation, a non-merger channel that preserves disk components in quenched galaxies (such as starvation or the creation of a halo shock) is favored over a major-merger scenario that builds bulge mass first while the SFR declines. This figure shows just one slice of the multivariate space to be explored in HSC. In addition, the superior image quality at Subaru allows for a range of structural and morphological parameters to be included, vastly increasing our ability to find and test physical scenarios.

4) How do galaxy sizes and morphologies evolve? One of the most exciting discoveries over the past few years is that elliptical galaxies at fixed mass were *smaller* than they are today by factors of two to four (van Dokkum et al. 2008), as recently as $z \approx 1$. With HSC, we can ask whether size evolution proceeded differently for ellipticals with different star formation histories or stellar mass, and whether size growth proceeds differently in clusters, where galaxies have been found to be as compact at lower-z as those at $z \sim 2$ (Valentinuzzi et al. 2010). It is thought that galaxies grew since $z \sim 1$ via minor merging, with accreted material from small "fluffy" galaxies remaining mostly at the outskirts of their massive hosts (Naab et al. 2009). We will test this by directly tracking the color evolution in the outskirts of massive elliptical galaxies out to $z \sim 1$, both individually and through stacking (e.g. Tal & van Dokkum 2011). If the outskirts are built via the accretion of small galaxies, the color gradients should grow bluer at later times. We can also compare the observed growth to the inferred minor merger rates (see above) for galaxies with the same mass and morphology.

4.3 How does the relationship between galaxies and dark matter halos evolve?

The processes regulating galaxy growth and assembly as described above are intimately tied to and driven by the growth of dark matter halos, which we can probe with gravitational lensing up to $z \simeq 1.4$ (Figure 4). We will measure the stellar-to-halo mass relation (SHMR, Figure 8) which tracks the average halo mass of central galaxies in each halo as a function of their observed stellar mass. When combined with measurements of clustering on small scales, the stellar-to-halo relation for satellites can simultaneously be constrained as well. Current studies (e.g., Mandelbaum et al. 2006, Moster et al. 2010, Leauthaud et al. 2012) suggest that the efficiency of stellar mass growth at $z \sim 0$ depends strongly on halo mass, peaking at $M_{\rm halo} \sim 10^{12} M_\odot$ (the "pivot" mass scale, corresponding to a stellar mass of $\sim 10^{11}\ M_\odot$). HSC will measure the SHMR from $z = 0.2$ ($M_* > 10^{8.8} M_\odot$) to $z = 1$ ($M_* > 10^{10.4} M_\odot$) using a combination of galaxy-galaxy lensing and the angular clustering of galaxies. HSC is expected to improve the current precision of the constraints on the SHMR by a factor of 10 with a near-vanishing sample variance. This will allow us to determine the

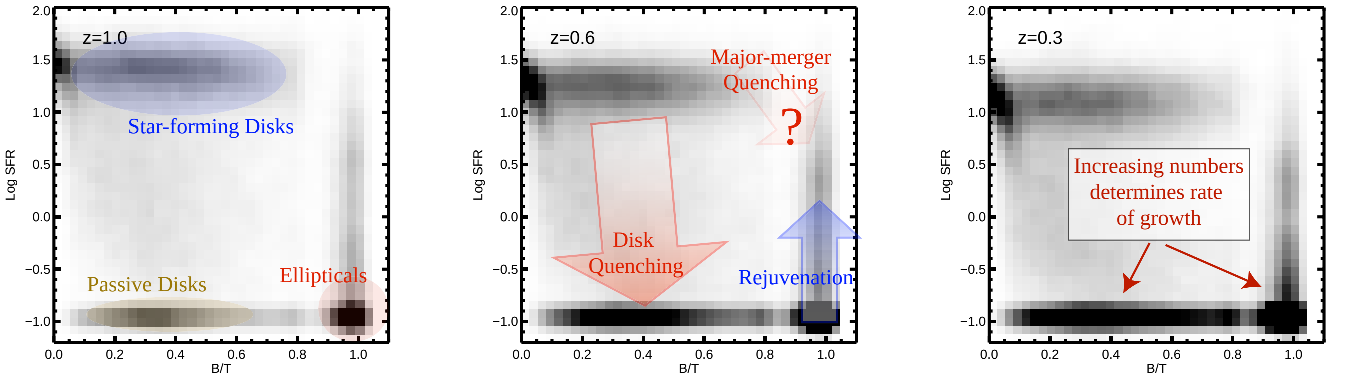

Figure 7: Mock HSC flow diagrams. The correlation between star formation rate and bulge-to-disk (B/T) ratio of galaxies from the Millennium Simulation selected in a narrow stellar mass bin centered at $M_* = 10^{11} M_\odot$, with increasing time from left panel to right. B/T will be well measured at low redshift and can be related to concentration (which can be measured at higher redshifts). The redshift evolution of this diagram demonstrates how HSC data will allow us to track how galaxies "flow" within this parameter space. Annotations in the left panel identify specific populations. The middle panel illustrates how various physical processes drive flows in this space. The lack of objects in the upper-right portion shows that ellipticals are not formed by major mergers of disks. Much more common is "disk quenching" of satellites as they fall into larger halos, with some evidence for rejuvenated star formation in ellipticals. We see in the right-hand panel that the relative fractions of different populations have evolved significantly. Measuring the evolving numbers of galaxies in different populations in such diagrams constructed for many redshift slices will constrain their rate of growth along various pathways.

precise redshift evolution of the pivot mass which, in combination with dark matter halo growth derived from numerical simulations, provides fundamental insight on how the regulation of star formation is tied to the growing dark matter halo.

4.4 Galaxy evolution in extreme environments

The Wide layer will provide a unique sample of ∼20,000 massive clusters with redshifts $z \lesssim 1.4$ and masses above $10^{14} M_\odot$. We will study the cluster galaxy populations as a function of cluster mass using statistical background subtraction to distinguish members from the field. Our large sample will not only elucidate signatures of quenching and morphological changes, but determine whether the SFR-mass relation for star-forming galaxies is altered in dense environments. This will reveal whether environmental mechanisms include gradual processes (e.g., strangulation or interruption of gas streams) or are primarily fast-acting (e.g., ram-pressure stripping). We can place the results in context by using halo mass estimates (via weak lensing, and in some cases from ACTPol SZ and eROSITA X-ray measurements) to statistically link clusters at different epochs by comparing to expected growth in cosmological simulations.

Most galaxy formation models (e.g., de Lucia et al. 2007) predict that the brightest cluster galaxies (BCGs) acquired nearly half of their final mass below $z \sim 0.5$. However, it is far from clear that there are enough mergers at late times to drive this growth. In addition, there is evidence for BCGs in massive clusters at $z \sim 1$ (e.g., Collins et al. 2009) which appear to be fully formed. The HSC sample of a statistically linked evolutionary cluster sequence will help determine when BCGs finish evolving by tracking BCG growth at late epochs.

5 Galaxy and Quasar Studies at High Redshift

Our HSC survey will also probe the epoch of galaxy *formation* at $z > 2$, when cosmic SFR rose with cosmic time. Suprime-Cam has led the world in wide-field studies of high-redshift galaxies, and has unveiled the evolution, clustering, environments, and physical properties of Lyman-break galaxies (LBG), Lyman-α emitters (LAE), and Lyman-α blobs (LAB) from $z \sim 2$ to $z \sim 7$. With the much larger field of view of HSC, we will address the next generation of key questions in the field, which require going deep over substantially larger solid angles with both broad-band and narrow-band (NB) filters. In particular, the NB component of our survey is unique: no other existing or planned wide-field survey is doing or will do NB imaging.

The detailed design of our Deep and Ultradeep layers is described below in Section 7; see especially Table 8. The broad-band depths are designed to select LBGs over the full redshift range $2 < z < 7$, as well as to detect the continuum in LAEs at all redshifts probed by the NB data. The depths and solid angles

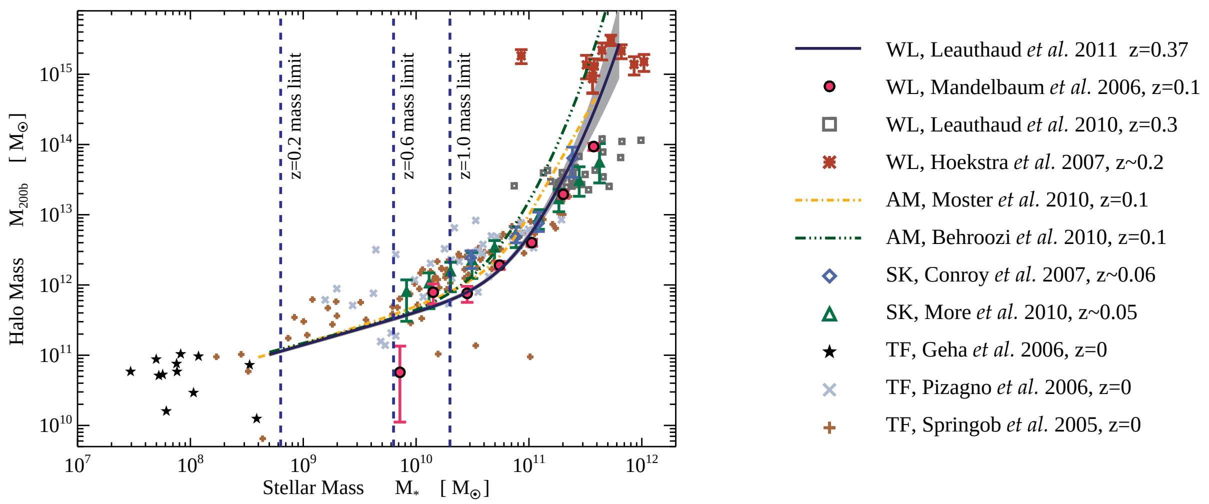

Figure 8: The low redshift stellar-to-halo mass relation (SHMR) as probed by WL, abundance matching (AM), satellite kinematics (SK), and Tully-Fisher (TF) estimates. A key feature in the SHMR is the "pivot mass" scale at $M_* \sim 10^{11} M_\odot$ where the quenching of star formation in massive galaxies causes the SHMR to bend sharply upwards. The dashed blue vertical lines show the stellar mass completeness limits of the HSC survey at $z = 0.2$, $z = 0.6$, and $z = 1.0$, demonstrating that HSC will be able to probe the redshift evolution of the pivot mass scale out to $z = 1$. Measurements of this pivot mass scale out to $z = 1$ should yield insights into the mechanisms that cause the quenching of star formation.

will allow us to accurately measure the clustering and luminosity functions of these populations. In the Ultradeep layer, the z and y filters will reach to L^* at $z \sim 7$, allowing the selection of dropout galaxies. With the NB filters, we will study the evolution of the properties of LAEs to $z = 7.3$, the nature of LABs, and the neutral hydrogen fraction and the topology of reionization at $z \sim 6 - 7$.

The Lyman-break and narrowband-excess techniques are well established, and we will need spectroscopic confirmation for only a small fraction of our objects (except for the rare objects at $z \gtrsim 7$), meaning that followup spectroscopy will not be a bottleneck in our study. PFS is designed to carry out more detailed studies of well-defined populations identified in this survey. Tables 5 and 6 show the expected numbers of LBGs and LAEs for the three layers calculated from the observed luminosity functions (LFs), mostly taken from our own studies with Suprime-Cam, with an extrapolation toward lower luminosities where needed. Each sample at each redshift is designed to address at least one key science goal.

Table 5: LBG samples

sample	BX/BM^a	u-drop^a	g-drop	r-drop	i-drop	z-drop	y-drop^b
redshift	2.3 ± 0.5	3.0 ± 0.5	3.8 ± 0.5	5.0 ± 0.5	5.9 ± 0.5	6.8 ± 0.5	7.8 ± 0.3
$N^c_{\rm UD}$	0.9M	0.22M	0.24M	50k	11k	700	2
$N^c_{\rm D}$	0.8M	98k	1.1M	0.2M	34k	99	0
$N^c_{\rm W}$	–	–	17M	1.9M	38k	4	–
$V^d_{\rm UD}$	16	16	15	14	12	11	2.6
$V^d_{\rm D}$	129	129	122	108	98	89	24
$V^d_{\rm W}$	–	–	6100	5400	4900	4450	–
$M^e_{\rm UD}$	$-18.0/-17.0$	-18.3	-18.2	-19.0	-19.9	-20.6	-21.6
$M^e_{\rm D}$	-19.5	-20.8	-18.8	-19.6	-20.4	-21.6	-24.1
$M^e_{\rm W}$	–	–	-19.8	-20.6	-21.6	-22.5	–
science^f	GE	GE	GE	GE	GE	GE, CR	CR

Notes – $^{a)}$Using CFHT u^* images for the Deep layer ($u^* = 25 - 25.5$ mag) from the archive and the Ultradeep layer ($u^* = 27 - 27.5$) from the on-going Foucaud et al. program. $^{b)}$$y$-dropouts identified by the combination of HSC, VISTA, and UKIDSS data in the Ultradeep fields. $^{c)}$Expected number of LBGs in each redshift slice. $^{d)}$The comoving volume of each redshift slice in units of $10^6 (h^{-1}{\rm Mpc})^3$. $^{e)}$Limiting absolute AB magnitude of the sample at rest frame 1300–1500Å. $^{f)}$Key science cases. GE: galaxy evolution in dark halos (Section 5.1), CR: cosmic reionization (Section 5.4).

Table 6: LAE and LAB Samples

narrow-band	NB387	NB816[a]	NB921[a]	NB101[a]
redshift	2.18 ± 0.02	5.71 ± 0.05	6.57 ± 0.05	7.30 ± 0.04
$N^b_{\rm UD}$	–	3.9k (60)	1.7k (30)	39 (0)
$N^b_{\rm D}$	9.0k (730)	14k (360)	5.5k (100)	–
$V^c_{\rm UD}$	–	1.2	1.2	0.79
$V^c_{\rm D}$	6.0	9.6	9.8	–
$L({\rm Ly}\alpha)^d_{\rm UD}$	–	1.5	2.5	6.8
$L({\rm Ly}\alpha)^d_{\rm D}$	2.7	2.9	4.1	–
science[e]	LA	LA, CR	LA, CR	LA, CR

Notes – [a)] We will use these narrow-band data down to the 4σ limits, following the convention in the literature. [b)]Expected number of LAEs, with numbers of LABs in parentheses, in each redshift slice. [c)]The comoving volume of each redshift slice in units of $10^6(h^{-1}{\rm Mpc})^3$. [d)]Limiting Lyα luminosity in units of 10^{42} erg s^{-1}. [e)]Key science cases. LA: evolution of LAEs and LABs (Section 5.2), CR: cosmic reionization (Section 5.4).

5.1 Galaxy evolution in dark matter halos

As described in Section 4.2, understanding the physics of galaxy evolution must be done in the context of the dark matter halos in which galaxies lie. We will measure dark-halo masses for galaxy populations by fitting Halo Occupation Distribution (HOD) models to the angular correlation function (ACF), constraining the relationship between galaxies and dark halos as a function of cosmic time from the reionization era to $z \sim 2$, which links smoothly with the weak lensing analysis of intermediate-z galaxies described in Section 4.

We will use the LBG samples over $2 < z < 7$ from the three layers to determine the dependence of SFR and stellar mass (M_*) on halo mass ($M_{\rm halo}$) over $M_{\rm halo} \sim 10^{11}M_\odot - 10^{13}M_\odot$. The Wide data are essential to identify the rare, highest-mass halos that existing studies (e.g., Foucaud et al. 2003; Ouchi et al. 2004; Lee et al. 2009; McLure et al. 2009) do not have the solid angle to discover, while the Deep and Ultradeep layers will probe to low masses and to the initial stages of mass assembly at $5 < z < 7$. SFRs will be derived from the observed far-UV luminosities for all galaxies. For galaxies in the Ultradeep layer and over 60% of the Deep layer (COSMOS, XMM-LSS and ELAIS-N1), we will use deep NIR data (Table 10) to derive their M_* and ages by stacking, if necessary, down to mass scales of dwarf galaxies, $\sim 10^7M_\odot$. For the remaining two Deep fields, we will estimate M_* from SFRs using the SFR–M_* relation to increase the statistics.

Figure 9 compares the observed $M_*/M_{\rm halo}$–$M_{\rm halo}$ relation with those predicted for $z < 2$ (Foucaud et al. 2010; cf., Figure 8). With the increased dynamic mass range of our sample ($10^{11} - 10^{13}M_\odot$), we will be able to detect the predicted peak at $M_{\rm halo} \approx 10^{12}M_\odot$ (de Lucia & Blaizot 2007), testing models of fueling and quenching mechanisms as a function of redshift. The dependence of M_* and SFR on $M_{\rm halo}$ revealed by our study will allow us to understand the observed SFR - M_* sequence (Daddi et al. 2007) in terms of physical models of structure formation. At least 1×10^4 galaxies are needed to constrain HOD models; our sample will be large enough to do so in multiple bins of redshift, luminosity and/or stellar mass. We will constrain the average number of galaxies hosted in dark halos and the star formation (SF) duty cycle, both of which are important parameters related to galaxy merging and stochastic SF. At $z \sim 7$, we will not be able to measure the 1-halo term, but we will measure the ACF on larger scales for the first time, constraining SF in dark halos in the reionization era.

5.2 Evolution of LAEs and LABs

LAEs are on average less massive and less obscured than LBGs (e.g., Ono et al. 2010), and they evolve very differently from LBGs, becoming more common at higher redshift (e.g, Ouchi et al. 2008). However, clustering studies to date are not large enough to measure the 1-halo term (Ouchi et al. 2010, Guaita et al. 2010). Our LAE samples will have the sensitivity to determine dark halo masses and galaxy distributions in them for the first time at $z = 2.2, 5.7$ and 6.6, comparing the results directly with those for the LBGs in the context of the analysis of Figure 9.

Stacked narrow-band images of LAEs in our sample may reveal diffuse Lyα (and UV) halos extending out to the virial radii of dark halos ($\sim 100\,$kpc: Steidel et al. 2011, Matsuda et al. 2012), allowing us to explore the interaction (both infall and outflow) of galaxies with ambient baryonic gas, as a function of dark

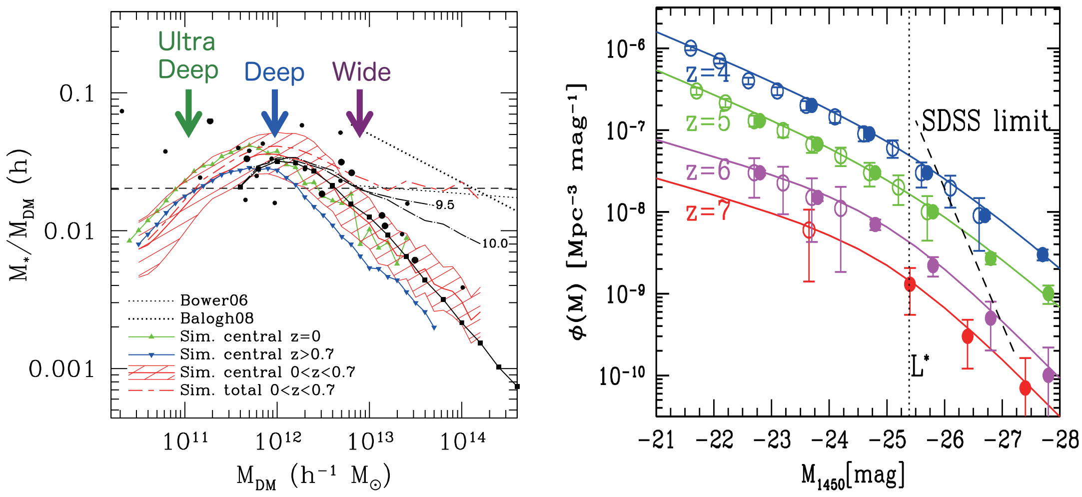

Figure 9: *Left*: Relation between $M_*/M_{\rm halo}$ and $M_{\rm halo}$ at $z < 2$. Compare with the low-redshift version shown in Figure 8. Combining data from the three layers will accurately determine this relation at $z > 2$ by bracketing the pivot mass at $M_{\rm halo} \approx 10^{12} M_\odot$. *Right*: Expected quasar LF over $z \sim 4-7$ with our HSC data. The filled and open circles correspond to the Wide and Deep layers, respectively.

halo mass and environment from our clustering analyses (Matsuda et al. 2011, 2012). For individual objects in which extended gas is detected, we will determine whether inflows occur along large-scale filaments by correlating their position angles to the background filaments traced by LAEs.

Individually detected Lyα halos ($\gtrsim 20\,$kpc), LABs, are very rare objects, possibly tracing very massive systems (e.g., Uchimoto et al. 2008) or short-term aspects of galaxy-formation processes (e.g., Saito et al. 2008). Even the HETDEX survey (Hill et al. 2010) will not be able to discover such objects, given its 1/7 fill factor. We predict that there will be of order 1000 LAB in our narrow-band imaging (Table 6). At $z = 2.2$ alone, we expect to discover 700 such objects, enough to measure their clustering, which will allow us to place them in the framework of structure formation.

5.3 Quasars and active galactic nuclei

The quasar phenomenon is a key aspect of galaxy formation: it marks the growth of the central supermassive black hole (SMBH), and must be related to galaxy evolution overall given the observed correlation between host galaxy and SMBH properties in the present-day Universe. The SDSS quasar sample is the largest survey of quasars to date, but it samples only a narrow range of luminosity at each redshift, does not have the depth to probe the galaxy population corresponding to quasar hosts at any but the lowest redshifts, and cannot probe above $z = 6.4$ because of the red limit of its filter set. HSC will be effective in pushing beyond these limitations. With the HSC data, we will select quasars via their colors (Richards et al. 2002), matching to infrared and X-ray data (Table 10) and via variability (Morokuma et al. 2008). Table 7 summarizes the number of objects that we expect to find. In the Wide layer, we will detect 280 $z \sim 6$ quasars (10 times more than SDSS) and 50 $z \sim 7$ quasars, thanks to the deep z- and y-band data. Variability selection is sensitive to even quite low-luminosity AGNs that are missed by other techniques; the cadence in the Deep broad-band data is well-matched to quasar variability timescales. We predict of order 200 (50) low-luminosity $z \sim 4$ ($z \sim 5$) quasars in the Deep layer, and 2000 at $z \sim 1$. In addition, we will detect a few $z \sim 7$ low-luminosity quasars, which are important to measure the faint end of the luminosity function, and will allow us to distinguish between models for quasar evolution and reionization. The colors lead to excellent photometric redshifts, especially at redshifts above 3, where the Lyα forest gives a distinctive signature in the colors as a function of redshift.

Table 7: Quasar Samples

	Wide (1400 deg^2)				Deep (27 deg^2)			
redshift	3.7–4.6	4.6–5.7	5.9–6.4	6.6–7.2	< 1	3.7–4.6	4.6–5.7	6.6–7.2
mag. range	$r < 23.0$	$i < 24.0$	$z < 24.0$	$y < 23.4$	$i < 25.0$	$i < 25.0$	$i < 25.0$	$y < 25.3$
number	6000	3500	280	50	2000	200	50	3

Evolution of supermassive black holes: The bright end of the quasar LF ($M_{\rm UV} < -26$) is well-fit with a power law whose normalization peaks at $z \sim 3$ (Richards et al. 2006). At lower luminosities, the optical LF shows a break from a pure power-law (e.g., Croom et al. 2009), but this break is very poorly measured at $z > 3$, where SMBH are actively growing, and where different feedback models make quite different predictions for the LF shape (Ikeda et al. 2011). With HSC, we will measure the overall shape of the quasar LF up to $z \sim 5$ for the first time, probing well below the break. Specifically at $z = 4 - 6$, we will detect quasars down to $M_{\rm UV} \sim -22.5$ in the Wide fields through the color selection, and down to $M_{\rm UV} \sim -21.5$ in the Deep fields via their time variability (right panel of Figure 9). While high-luminosity quasars may be accreting at close to the Eddington rate, the lower-luminosity objects are likely to be undergoing a different mode of accretion, which can be probed with detailed measurement of the LF shape.

Clustering properties and environments of quasars: With precisely measured spatial clustering of quasars (and the galaxies around them) as a function of luminosity, one can infer the masses of hosting halos, the locations of quasars in the halos, and (with the LF measurements above) quasar duty-cycles, all of which are crucial to constrain models of the growth mechanisms of quasars, especially at $z > 3$ and at low luminosities. We will examine the properties of galaxies in the vicinity of quasars to search for large-scale feedback effects from the quasars. Combining our quasar sample with galaxy samples from the same imaging data, we will evaluate large-scale effects with much improved statistics than has been done to date (e.g., Kashikawa et al. 2007) to constrain galaxy evolution models.

Relationship of AGN to their host galaxies: The superb imaging afforded by HSC allows us to study the host galaxy properties of the $z < 1$ AGN, including their stellar masses, star formation rates and morphologies. The number density of moderate-luminosity AGNs peaks at $z \sim 1$; it is unknown whether these sources are dominated by massive elliptical galaxies whose nuclear activity is shutting down, or smaller black holes undergoing major growth episodes (i.e., dust-obscured starbursts). If AGN activity is responsible for star-formation quenching, we might expect AGN to appear in transitioning galaxies, such as those undergoing merging (e.g., Hopkins et al. 2006b). We will explore the morphologies and colors of hosts using our variability-selected low-luminosity AGNs and X-ray-selected type-2 AGNs in the HSC Deep layer.

5.4 Cosmic reionization

As we probe further back in cosmic time, we reach the epoch of cosmic reionization, when the formation of the first galaxies described above reionized the intergalactic medium. Our HSC observations will address three of the current biggest questions in the study of cosmic reionization: (i) when did it take place? (ii) what was the topology of reionization? (iii) what are the ionizing sources responsible for the transition?

While the Gunn-Peterson test (Gunn & Peterson 1965) from the spectra of distant quasars suggests an increase in the neutral fraction of the intergalactic medium (IGM), $x_{\rm HI}$, beyond $z \sim 6$ (Fan et al. 2006), the CMB polarization data from WMAP rule out instantaneous reionization below $z = 8.2$ (6.7) at the 2σ (3σ) level (Dunkley et al. 2009). Thus reionization probably occurred over a range of epochs, and is predicted to have been spatially quite inhomogeneous (e.g., McQuinn et al. 2008).

Reionization epoch and topology: LAEs are a powerful probe of the IGM neutral fraction $x_{\rm HI}$ during reionization. Neutral hydrogen in the IGM scatters Lyα photons from LAEs, leading to evolution of the observed Lyα LF (e.g., Malhotra & Rhoads 2004; Kashikawa et al. 2006; Iye et al. 2006; Ota et al. 2008; Ouchi et al. 2010; see the left panel of Figure 10). Measurements of the LF as a function of position can thus constrain the reionization history, and measure the reionization topology due to the high surface density of LAEs. Studies to date are limited by the small solid angles of existing samples, and the paucity of LAEs at $z \gtrsim 7$.

With our large sample of LAEs from the Deep and Ultradeep layers (Table 6), we will construct the Lyα LFs at $z = 5.7$, 6.6, and 7.3, and determine the evolution of the Lyα LF at the $> 3\sigma$ level up to $z = 7.3$ (Figure 10). At $z = 5.7$ and 6.6, the Ultradeep data are deep enough to detect LAEs significantly fainter than L^* (the two separate fields mitigate cosmic variance), while the Deep layer is sensitive to the high-luminosity end of the LF. With the Ultradeep data, we will increase the number of known LAEs at $z = 7.3$ by an order of magnitude; the resulting LF will give the first meaningful constraint on $x_{\rm HI}$ beyond $z = 7$. The SEDs of these objects, obtained by stacking the multi-band data from optical to mid-infrared (Table 10), will allow us to determine whether they have primordial features such as top-heavy IMFs or extremely low metallicities, which would affect the production rate of ionizing photons.

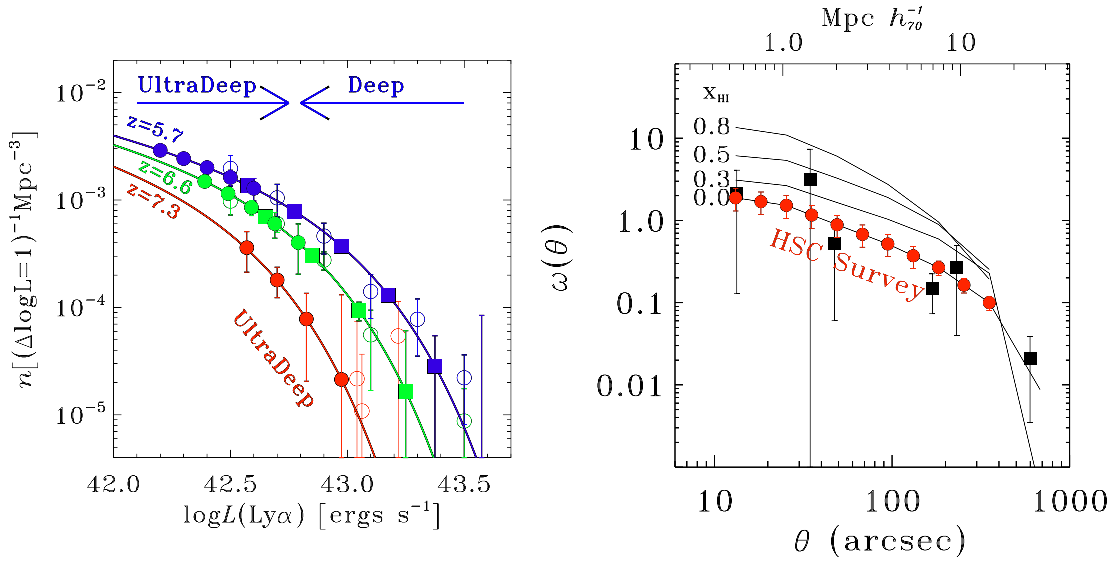

Figure 10: *Left*: Expected measurements of the Lyα LFs at $z = 5.7$ (blue), 6.6 (green), and 7.3 (red) with the Ultradeep and Deep layer data. The existing Suprime-Cam measurements at $z = 7.3$ go very deep, although over a very small area. The open circles are the current best measurements given by Suprime-Cam observations. The decrease in the LF with increasing redshift is interpreted as due to the onset of reionization. *Right*: Expected ACF $\omega(\theta)$ of $z = 6.6$ LAEs from the Deep layer in the case of full ionization, assuming that they are hosted by $M_{\rm halo} = 3 \times 10^{10} M_\odot$ halos (red dots). The solid curves indicate the ACFs of LAEs with $M_{\rm halo} = 3 \times 10^{10} M_\odot$ for $x_{\rm HI} = 0, 0.3, 0.5, 0.8$ taken from McQuinn et al. (2007) simulations of inhomogeneous reionization. The black squares are the best estimates of the $z = 6.6$ LAE ACF available to date (Ouchi et al. 2010). Our accurate ACF measurements over a range of a factor of 30 in θ will allow us to detect the difference in the ACF shape between the full and partial ionization cases and to constrain $x_{\rm HI}$ with an uncertainty of ~ 0.2.

The sample of $z = 5.7$ and $z = 6.6$ LAEs from the Deep layer will cover unprecedented solid angles, allowing us to detect the effect of ionized bubbles on the angular clustering. The solid angle of the Deep layer corresponds to 0.6 Gpc^2 and should include tens of ionizing bubbles, whose signature imprints a distinctive pattern in the ACF. This will allow us to infer $x_{\rm HI}$ with an accuracy of ~ 0.2 at $z = 6.6$ (Figure 10), and constrain models for the topology of reionization. Combining the LF and ACF results, we will obtain $x_{\rm HI}$ at $z = 6.6$ with a predicted precision of ± 0.1, and will constrain the physical nature of the objects causing the reionization. Spectroscopic follow-up of the high-redshift quasars we discover (Section 5.3) will allow us to explore the structure of the Gunn-Peterson absorption in three dimensions, further constraining the topology of reionization.

Finally, the Low Frequency Array (LOFAR) will probe the neutral hydrogen distribution at $z \sim 6-7$ (Zaroubi et al. 2012) over the HSC ELAIS-N1 Deep layer field. The cross-correlation function of the LOFAR data and HSC LAEs will reveal the signature of reionization and the evolution of ionized bubbles at the $\sim 5\sigma$ level (Lidz et al. 2009). We are in close communication with the LOFAR team for this cross-correlation analysis.

Reionizing sources: Star-forming galaxies are thought to be the principal sources of the ultraviolet photons that reionized the IGM at high redshift, but recent studies indicate a shortfall in UV photons from galaxies at $z \sim 6-7$ (e.g. Robertson et al. 2010). Ouchi et al. (2009) claim that galaxies are adequate to ionize the Universe at $z \sim 7$ only if $\alpha < -1.9$, where α is the faint-end slope of the LF. However, the current constraint on α is not strong enough to draw any firm conclusions.

Even the deepest *HST* imaging programs, such as CANDELS and UDF, do not probe far enough down the luminosity function of $z \sim 7$ galaxies to observe the bulk of the galaxies that are thought to be responsible for reionization. However, if we assume the LF has a Schechter-like power-law form at the faint end, we need to constrain the LF shape around the knee (L^*) to measure α from the *HST* data. Our HSC survey will contain 800 bright z-dropout galaxies with $M_{\rm UV} < -20.6$, providing just that constraint.

6 Ancillary Science

The science goals of the proposed survey are focused on cosmology and galaxy evolution. However, the lesson of all major surveys is that the data one gathers to carry out the main science goals can be used to enable breakthroughs in quite different areas of astronomy. The SDSS, for example, was designed originally to map the large-scale distribution of galaxies, but among its high-profile unanticipated discoveries were the coolest brown dwarfs (e.g., Strauss et al. 1999), streams in the Galactic halo (Belokurov et al. 2006), dark matter halo masses from the weak lensing signal from galaxies (Mandelbaum et al. 2006), and the properties of tens of thousands of small Solar System objects from detection of moving objects (Ivezić et al. 2001). We similarly anticipate that the HSC survey will enable significant discoveries in areas far removed from our core science goals. Among the opportunities are:

- Studies of transient and variable objects of all sorts. While Type Ia supernovae will be used as a cosmological probe, our survey will discover significant numbers of core-collapse supernovae as well, including significant numbers of superluminous supernova up to $z \sim 4$, and rare optical transients such as orphan gamma-ray burst afterglows. These data can be used to constrain the rate of supernova explosions with cosmic time, the distribution of the time between star formation and supernova explosions (which constrains models for the progenitors) and correlations with host galaxy properties. We are also particularly interested in discovering the shock-breakout event (which lasts a few hours) in supernova explosions; we predict that we may find several tens of shock-breakout events in the HSC data.
- Discovery of rare populations of asteroids in our Solar System. Perhaps the greatest discovery potential is in the Ultradeep layer, where the repeated cadence and great imaging depth will make us sensitive to faint trans-Neptunian objects, allowing us to measure orbits and measure light curves in multiple bands. In addition, discoveries of contact binaries and main belt comets are expected from the analysis of the PSF and moving properties of objects.
- The depth of the imaging allows main sequence stars to be seen to the outer Milky Way halo. The halo is thought to have been built up from the cannibalized debris of neighboring galaxies, and we predict 3-4 new stellar streams and of order 20 new ultra-faint dwarf galaxies in the Wide layer.

7 HSC Survey Design and Strategy

Having described the science drivers for the HSC survey, we now turn to a detailed description of the survey design that will allow us to reach our science goals. We describe our survey areas and depths of each filter in Section 7.1, our choices of fields in Section 7.2, and our detailed survey strategy in Section 7.3.

7.1 Filters and depths

The nature, depth, and solid angle of each filter for the HSC survey were carefully determined to meet the main science requirements. Tables 8 and 9 summarize the filters, depths and total requested exposure time for each survey layer. Here we describe the survey parameters for each layer, relating to the scientific goals described in detail in Sections 3, 4 and 5.

HSC-Wide layer: the primary science driver for HSC-Wide is WL cosmology, as detailed in Section 3. To meet the WL science goals, the **top-level survey requirements** are:

- To carry out i-band imaging (20 min in total per field) in nights of good seeing conditions (FWHM $\lesssim 0.7''$) in order to carry out high-precision measurements of the shapes of faint, distant galaxies. This depth gives us a weighted mean number density of galaxies for which shapes can be measured of $\bar{n}_g \simeq 20$ arcmin^{-2}, with $\langle z \rangle \simeq 1$.
- To combine the i-band data with other filter data ($grzy$) for the Wide layer to estimate photo-z's for every galaxy used in the WL analysis.
- To cover a solid angle of 1400 deg^2, which leads to our FoM requirement on WL observables.

With these data, we will recover the dark matter distribution with unprecedented statistical precision to higher redshifts than previously reached or can be reached with 4m-class telescopes. The statistical accuracies of our WL measurement will depend on the number density of galaxies usable for WL analysis and the total solid angle (which, given the redshift range of our sample, determines the total comoving volume covered by the survey). The i-band is ideal for measuring faint galaxy shapes, given the red colors of high-redshift galaxies, the high throughput and relatively low sky of the filter, and the good seeing. Twenty-minute i-band exposures with Suprime-Cam in $\lesssim 0.7''$ seeing yield a weighted number density of galaxies with measurable shapes for weak lensing analyses of about 20 galaxies/arcmin^2. With this exposure time, we go deep enough to probe WL to $z > 1$, allowing us in 200 nights to cover the cosmological volume necessary to attain our desired constraints on w and the DE FoM.

The total exposure time is split into 6 exposures for each field, and includes a single 30-second exposure to allow the photometry of each field to be tied to SDSS with bright stars (see Section 8.1). We will

Table 8: Filters and Depths

Layer	Filter	Exp.^{a} (# of epochs)	Lim. mag.^{b} (5σ, $2''$)	Moon^c phase	Requirement(s)^d	Main scientific driver(s)^e
Wide	g, r	10 min (3)	26.5, 26.1	d	photo	photo-z, $z \lesssim 2$ gals, QSO
Wide	i	20 min (6)	25.9	d	FWHM $\lesssim 0.7''$	WL, $z \lesssim 2$ gals, QSO
Wide	z, y	20 min (6)	25.1, 24.4	g	photo	photo-z, clusters, $z \sim 1$ gals, $z \sim 6$–7 QSO
Deep	g, r	1.4 hrs (10)	27.5, 27.1	d	cadence	SNeIa
Deep	i	2.1 hrs (10)	26.8	d	FWHM $\lesssim 0.7''$, cadence	WL calibration, SNeIa
Deep	z	3.5 hrs (10)	26.3	g	cadence	$z \lesssim 2$ gals, ionization topology, SNeIa, QSO
Deep	y	2.1 hrs (10)	25.3	g	cadence	$z \lesssim 2$ gals, SNeIa, QSO
Deep	$N387$	1.4 hrs ($\simeq$10)	24.5	d	photo	$z \simeq 2.2$ LAEs & LABs
Deep	$N816$	2.8 hrs ($\simeq$ 10)	25.8	g/d	photo	ionization topology, $z \simeq 5.7$ LAEs & LABs
Deep	$N921$	4.2 hrs ($\simeq$ 10)	25.6	g/d	photo	ionization topology, $z \simeq 6.6$ LAEs & LABs
UD	g, r	7 hrs (20)	28.1, 27.7	d	cadence	$z \gtrsim 2$ gals, SNeIa
UD	i	14 hrs (20)	27.4	d	cadence	$z \gtrsim 2$ gals, SNeIa, QSO
UD	z, y	18.9 hrs (20)	26.8, 26.3	g	cadence	$z \gtrsim 2$ gals, SNeIa, QSO
UD	$N816$	10.5 hrs ($\simeq$ 10)	26.5	g/d	photo	$x_{\rm HI}(5.7)$, $z \simeq 5.7$ LAEs & LABs
UD	$N921$	14 hrs ($\simeq$ 10)	26.2	g/d	photo	$x_{\rm HI}(6.6)$, $z \simeq 6.6$ LAEs & LABs
UD	$N101$	17.5 hrs ($\simeq$ 10)	24.8	g/d	photo	$x_{\rm HI}(7.3)$, $z \simeq 7.3$ LAEs

Notes – $^{a)}$ The total exposure time for each filter and the number of epochs over which the exposure will be split. The exposure times listed are the effective exposure time without accounting for weather losses. $^{b)}$ The expected 5σ limiting magnitude for a point source ($2''$ diameter aperture) under optimal conditions. PSF magnitude limits for point sources are 0.3 mag deeper than the numbers quoted in the table, but about 0.3 mag is lost when taking into account airmass effects. $^{c)}$ The moon phase for each filter imaging; gray (g) or dark (d) nights. $^{d)}$ The primary requirement on each filter imaging: photometric conditions (photo), good seeing conditions or cadence (for SN light curves and quasar variability). $^{e)}$ The primary science drivers for imaging in each filter. LBGs, LAEs, and LABs refer to Lyman-break galaxies, Lyman-α emitters, and Lyman-α blobs, respectively, and $x_{\rm HI}(z)$ is the neutral hydrogen fraction.

dither the exposures by ~ 0.6 degrees to make the exposure coverage more uniform. The exposures will be separated by at least a day, so that every star and galaxy are observed at different positions on the focal plane and under different atmospheric conditions. This strategy allows us to quantify and ameliorate systematic effects inherent in the shape measurement (Section 3.4).

The photo-z information, obtained from the combined data ($grizy$), is crucial for studying the evolution and nature of intermediate-redshift galaxies at $z \lesssim 2$ compared to the benchmark results of SDSS galaxies at $z \sim 0$. The photo-z's allow us to study the WL signals as a function of redshift, and to carry out WL tomography, which significantly improves constraints on cosmological parameters (see Section 3). The depths in each filter are chosen to optimize the measurements of photo-z's for galaxies up to $z \sim 1.5$. As in the i-band, we split the exposure of each filter into 3-6 visits, and dither, in order to maintain uniformity.

HSC-Deep/Ultradeep layers: The primary science drivers for the Deep and Ultradeep (UD) layers are fivefold: (1) to constrain the physics of growth, star formation quenching, and mass assembly of galaxies at $z < 2$; (2) to study the halo mass dependence of star formation and stellar mass assembly up to $z < 7$ from clustering and WL analyses; (3) to understand the physical processes of cosmic reionization from measurements of the IGM neutral fraction and its spatial inhomogeneity up to $z = 7.3$; (4) to study the evolution of faint quasars at all redshifts; (5) to probe the cosmic expansion history via the luminosity-distance relation using lightcurves of ~ 120 SNeIa up to $z \simeq 1.4$. The knowledge on galaxy properties obtained from the Deep/Ultradeep data will be used to calibrate photo-z's and shape measurements for the HSC-Wide WL cosmology. In addition, the repeated observations will allow us to diagnose systematic errors in the PSF/galaxy shape measurements. To meet the scientific goals, the **top-level survey requirements** for the HSC Deep/Ultradeep layers are:

- To use the broad- and narrow-band filter images in the proposed depths, as given in Table 8, in order to identify a sufficiently large number of LBGs, LAEs and LABs at the target redshifts, allowing us to measure the luminosity function and the two-point correlation functions to the desired precision at each redshift (see Section 5 for details).
- To observe in the broad-band filters in the Ultradeep fields with a cadence optimized to identify SNeIa at high redshift up to $z \simeq 1.4$ as well as other intriguing transients such as superluminous supernovae and gamma-ray burst afterglows.
- To go deep enough in the broad-band filters ($grizy$) for Deep to obtain good photo-z estimates of every

Table 9: Total exposure time and overhead

Layer/Comp.	filter	Exp./field [min]	Unit. exp. [min]	# of fields[a]	Total exp. [hrs]	Total readout[b] [hrs]	Subtotal[c] [hrs] (nights)
Wide	g	10	3.3	916	152.7	22.1	
	r	10	3.3	916	152.7	22.1	
	i	20	3.3	916	305.3	44.3	
	z	20	3.3	916	305.3	44.3	
	y	20	3.3	916	305.3	44.3	
					1221.2	177.1	1398.3 hrs (155.4 nights)
Deep	g	84	4	15	21	2.54	
	r	84	4	15	21	2.54	
	i	126	6	15	31.5	2.54	
	z	210	6	15	52.5	4.23	
	y	126	6	15	31.5	2.54	
	N387	84	21	15	21	0.48	
	N816	168	21	15	42	0.97	
	N921	252	21	15	63	1.45	
					283.5	17.3	300.8 hrs (33.4 nights)
Ultradeep	g	420	4	2	14	1.69	
	r	420	4	2	14	1.69	
	i	840	6	2	28	2.25	
	z	1134	6	2	37.8	3.04	
	y	1134	6	2	37.8	3.04	
	NB816	630	21	2	21	0.48	
	NB921	840	21	2	28	0.64	
	NB101	1050	21	2	35	0.8	
					215.6	13.6	229.2 hrs (25.5 nights)
Filter exch.[d]	0.25 [hrs] × 2 [times/night] × 227 [nights] ≃ 114 hrs						114 hrs
Subtotal[e]							2042 hrs (227 nights)
Calib. exp.[f]	*grizy*	0.5×5	0.5	920	38.3	37.1	75.4 hrs

Notes – The net exposure time and the overhead for each layer. [a)]The total number of fields to cover the area of each layer. We will dither around each field in each filter to improve photometric calibration. [b)]We assume 29 second readout overhead between exposures in a given field (see Table 2); the numbers shown are the total readout overhead in each band and each layer. [c)]To estimate the total number of requested nights, we assume that about 9 hours per night on average are available. [d)]For the filter exchange overhead, we assume that each filter exchange takes 15 minutes including the time for the telescope to slew to the zenith, each observing night has two filter exchanges, and we have a total of 227 clear observing nights. [e)]The total of 227 nights is estimated from the sum of the nights needed for the Wide, Deep and Ultradeep layers, including the filter-exchange overhead. [f)]"Calib. exp." refers to the 30-second calibration exposures we will take for each field in each filter to tie the HSC photometry to that of the much shallower SDSS (see Section 8.2). We assume that the calibration exposures can be taken under twilight or bad-seeing conditions.

galaxy down to $i \simeq 25$ ($\sigma_{dz/(1+z)} \simeq 0.04$ and less than 10% photo-z outlier rate) when combined with the deep NIR data available for two of the four target fields (Section 7.2).

As we emphasized in Section 5, the deep wide-field narrow-band imaging, in combination with deep broad-band imaging, is unique; no other 8m-class telescope is capable of doing this survey at all.

The proposed cadence of observations can be done within the SSP observation framework by mixing observations from the Wide, Deep and Ultradeep layers in the schedule (see Section 7.3 for details). The observations in each broad-band filter for the Ultradeep layer are split over 20 epochs. In the i- and z-bands, each epoch is 60 or 80 min long, needed to carry out $> 5\sigma$ photometry of $z = 1.4$ SNeIa one week before, and two weeks after, the peak of the lightcurve. The exposure of each broad-band filter for the Deep layer is split over 10 epochs. The single-epoch exposure time for the r-, g-, and i-bands allows us to do $> 5\sigma$ photometry of $z = 1 - 1.2$ SNeIa one week before, and two weeks after, the peak of the lightcurve. The cadence covers timescales ranging from a day to a few months, and the single-epoch depths match requirements to identify transients at high redshift beyond the reach of 4m-class telescopes (see the right-lower panel of Figure 12).

7.2 Survey fields

Table 10 and Figure 11 summarize the target fields for the HSC-Wide, Deep and Ultradeep layers. We impose the following requirements for the survey field selection:

- The HSC footprints should overlap the SDSS/BOSS footprint, because we use the SDSS for baseline photometric and astrometric calibration of the HSC data (Section 8.1). The BOSS data will provide a huge spectroscopic sample of galaxies up to $z \sim 0.7$, which will be used to calibrate photometric redshifts and the cluster-finding algorithm, and will be used for cosmological analyses.

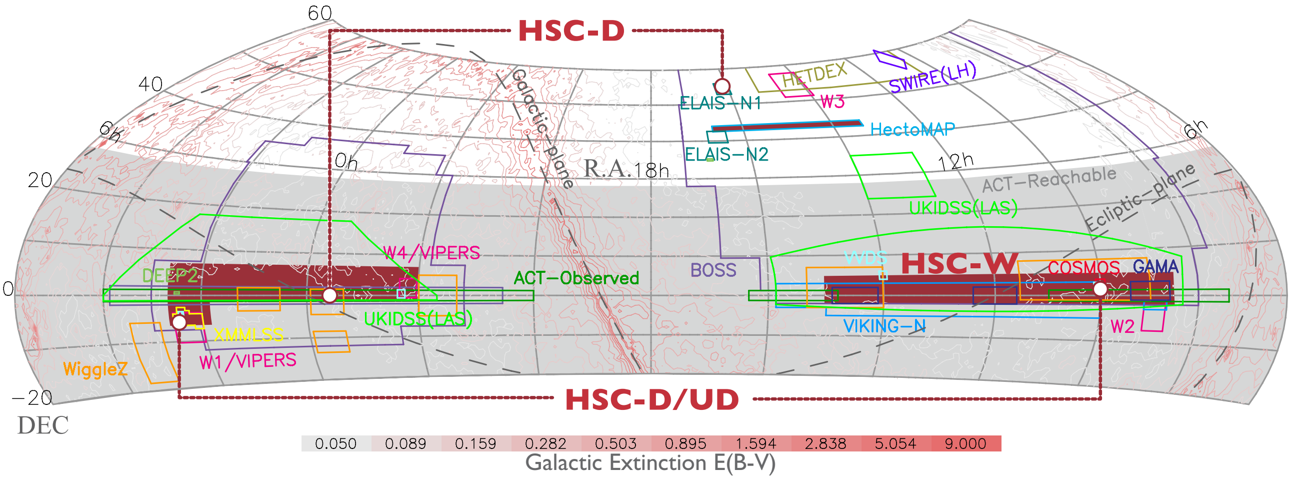

Figure 11: The location of the HSC-Wide, Deep (D) and Ultradeep (UD) fields on the sky in equatorial coordinates. A variety of external data sets and the Galactic dust extinction are also shown. The shaded region is the region accessible from the CMB polarization experiment, ACTPol, in Chile.

Table 10: Survey Fields

Layer	Name	RA, Dec	Area [deg^2]	Key Other data
Wide	Fall equatorial	22:00≤RA≤02:40 & -1°≤Dec≤ +7° 01:50≤RA≤02:40 & -7°≤Dec≤-1°	≃640	ACT(ACTPol), VIPERS, DEEP2, XMM, UKIDSS, WiggleZ
	Spring equatorial	08:30≤RA≤15:00 & -2°≤Dec≤+5°	≃680	ACT(ACTPol), VIKING/KIDS, UKIDSS, GAMA, Herschel
	Northern sky	13:20≤RA≤16:40 & +42.5°≤Dec≤+44°	55	spec-z (HectoMAP: $r < 21.3$)
Deep	XMM-LSS	02:25:00 -04°30′00″	5.3	UKIDSS-DXS(NIR), VIDEO-XMM-LSS(NIR), VVDS(spec-z), PRIMUS(spec-z)
	E-COSMOS	10:00:29 +02°12′21″	7.2	UKIRT/CFHT(NIR), VVDS(spec-z)
	ELAIS-N1	16:10:00 +54°00′00″	7.2	UKIDSS-DXS(NIR), LOFAR-Deep(radio)
	DEEP2-3	23:30:00 +00°00′00″	7.2	DEEP2(spec-z), PRIMUS(spec-z)
UD	SXDS/UKIDSS	02:18:00 -05°00′00″	1.8	UKIDSS-UDS(NIR), SpUDS(MIR), VVDS(spec-z), CANDELS(HST), PRIMUS(spec-z), UDSz(spec-z)
	COSMOS	10:00:29 +02°12′21″	1.8	UltraVISTA(NIR), CANDELS(HST) VVDS(spec-z), zCOSMOS(spec-z), PRIMUS(spec-z), Spitzer[a]

[a] We were recently approved for 1250 hours of warm Spitzer time for deep observations of the COSMOS field.

- The fields should be well distributed over a wide range of RA, such that fields are reachable at all times of the year.
- The fields should overlap other multi-wavelength data sets to maximize scientific potential when combined with the HSC data. The major data sets which offer unique synergy with HSC data are the arcminute-resolution, high-sensitivity CMB survey by ACT in Chile, and its polarization extension ACTPol, for which Princeton is playing a major role; X-ray surveys from XMM and eROSITA; near-/mid-infrared imaging surveys (e.g., VIKING/VIDEO and UKIDSS); and deep spectroscopic surveys (e.g., VIPERS, GAMA, COSMOS, HectoMAP).
- The Ultradeep regions should be included in the Deep fields, and (with one exception, see below) the Deep fields should be included in the Wide fields.
- The fields should be low in Galactic dust extinction.

One of our wide fields matches a unique 55 deg^2 region, the HectoMAP field, where Kurtz et al. (2012) are carrying out a spectroscopic survey for galaxies with $r < 21.3$ with Hectospec, a wide-field multi-object optical spectrograph, on the 6.5m MMT telescope. We will use the spatially-dense spectroscopic galaxy catalog to calibrate cluster finding methods for the Wide data.

Although it is not listed in Table 10, we will also obtain broad-band images in *grizy* for the All-wavelength Extended Groth Strip (AEGIS) field (RA $= 14^{\rm h}17^{\rm m}$, Dec $= +52°30'$) to the depths of the Deep layer. The AEGIS data is the largest field with publicly available densely sampled spectroscopic redshifts down to $R < 24.1$, including the DEEP2 and DEEP3 spectroscopic samples; this sample is key for calibrating photometric redshifts. The field can be observed with HSC with a single pointing, thus the

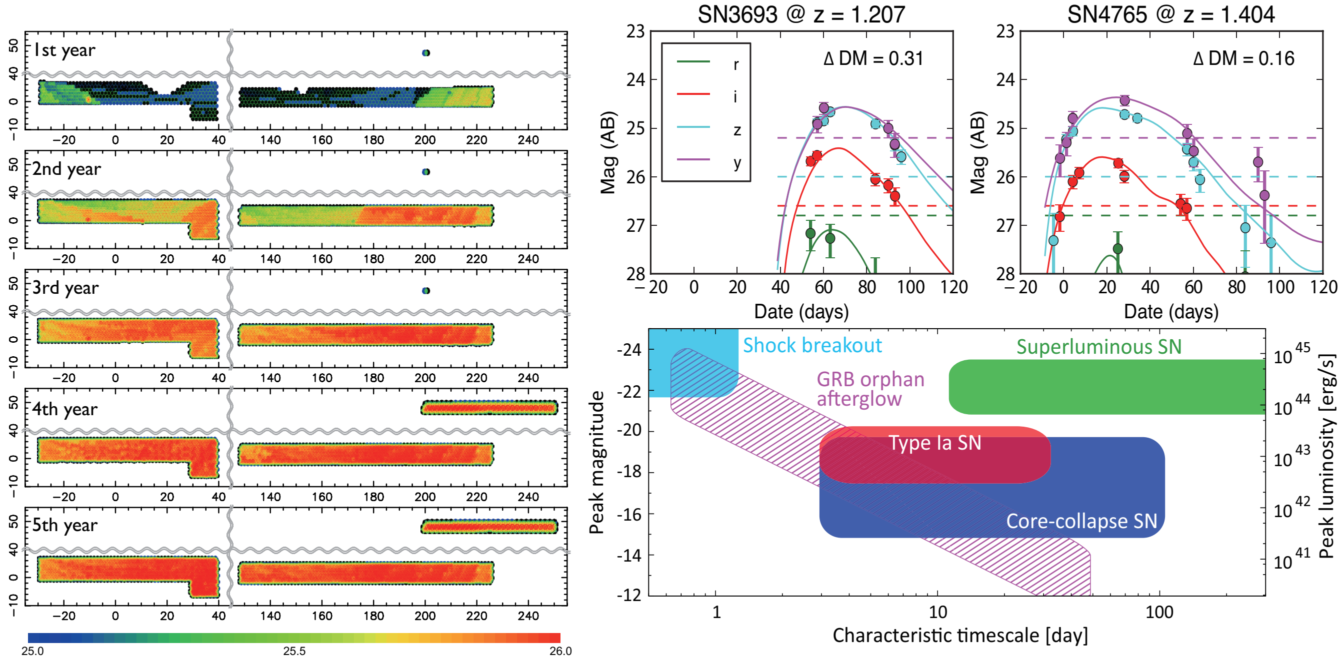

Figure 12: *Left*: An example of the results of survey simulations, showing how the i-band imaging for the Wide layer is built up over the five years of the survey. We consider six dithering pointings in each field. The color scales display the expected limiting magnitude for $2''$ aperture photometry for a point source in each field, taking into account the seeing, airmass, and sky brightness of each field. *Right-upper*: The expected sampling rate and photometric accuracy of lightcurves of SNeIa at various redshifts seen in the Ultradeep survey simulation. Each curve corresponds to a different filter. $t = 0$ corresponds to the beginning of the 4 month period that either one of the Ultradeep fields is observed. The quantity "ΔDM" shown in each panel is the expected 1σ error of the distance modulus for the simulated SNeIa, demonstrating that the sampling is adequate to measure distances. *Right-lower*: Typical bolometric absolute magnitude of various transients that will be found in HSC survey as a function of the characteristic timescale of variability.

broad-band imaging in all five bands requires less than a night of observing. We will observe this field early in the survey, or during commissioning if possible.

While it does not lie inside the Wide footprint, the ELAIS-N1 field of the Deep layer is also unique: it has deep NIR data (UKIDSS-DXS), and is one of the deep LOFAR survey fields.

7.3 Survey strategy

The unique opportunity of the Subaru SSP program allows us to carry out a very efficient survey interleaving the Wide, Deep, and Ultradeep layers. We use survey simulations to develop an optimal survey strategy within the SSP framework. We assume up to 6 nights every month, 60 nights per year and 300 nights in total for a 5 year survey. Our simulations include effects such as observing overheads (filter exchange, slewing time of the telescope, and the readout time of the camera), the elevation and location of each target field on a given night, the fact that the camera can hold up to six filters on a given run, the statistics of seeing and weather conditions at Mauna Kea (30% of the nights are assumed lost to weather), the airmass, and the moon phase and its location on the sky. We ran simulations using different cadences for the Deep and Ultradeep layers, and different priorities for covering the full footprint of the Wide layer uniformly from the beginning. Based on these simulations (Figure 12), we have settled on the following strategy:

- We request allocations of 5 non-contiguous nights for each month, with phases relative to new moon as follows: $(-6, -3, 0, +3, +6$ days) (14 runs) $(-5, -4, 0, +4, +5)$ (18 runs) and $(+2, +3, +4, +5, +6)$ (28 runs)[7].
- Our observations include a mixture of exposures for each of the three layers. The i-band filter is always in the instrument. There are up to three NB filters in at any given time.
- We carry out i-band imaging for the Wide/Deep fields when the seeing is better than FWHM$= 0.7''$.
- We observe only one of the Deep/Ultradeep fields in broad-band filters within a given month; this optimizes the cadence for supernova studies.

[7]This allocation is not a stringent requirement, and we will be flexible in scheduling our observing nights around open-use programs of HSC.

- The Deep fields include five overlapping pointings each. We will *not* coadd the narrow-band data in the overlaps, as the filter responses will be slightly different in different parts of the field.
- We allow no more than two filter exchanges per night to minimize the filter-exchange overhead.
- We carry out the redder band imaging when the moon is up (i-band imaging is allowed for fields $> 60°$ from the moon; zy can be done at any moon phase).

However, we would like to note that the survey strategy above is only our current working example. Depending on the quality of actual HSC data we will soon obtain from the commissioning runs, we will continue to explore an optimal survey design to maximize the science return consistent with our science requirements and goals. We plan to use the first year or so of data to write high-impact science papers, and will use this experience to refine our survey design. Table 9 gives details of the exposure time and overhead for each layer.

The left panel of Figure 12 shows one example of the survey simulation results, demonstrating that our strategy gives efficient and homogeneous coverage of the Wide survey area. We have carried out multiple survey realizations (differing in the random seeds for the seeing and weather conditions). These have demonstrated that our survey strategy robustly leads to more than 99% completeness on average for all three layers in all filters, for a 300 night survey. To be more quantitative, the completeness (observing time relative to the required total exposure time for our design depth) is: 99 ± 1.5, 99 ± 1.7, and $98 \pm 2.1\%$ for the Wide, Deep and Ultradeep layers, respectively, where the error bars are the 1σ scatters of 300 realizations averaged over filters. The right-upper panel of Figure 12 shows the expected lightcurves for SNeIa at different redshifts, taken from one realization of the survey simulations. Our cadence allows a sufficiently dense sampling in time to follow the lightcurve, which in turn enables us to reliably infer the luminosity distance based on the standard candle technique. We expect to find about 40 SNeIa at $z \geq 1$ in the Ultradeep layer, and 120 SNe in all.

Back-up observation plans: Because our photometric calibration is done relative to the dense network of standards from the SDSS survey (Section 8.2), we will be able to take survey-quality data in mildly non-photometric conditions. However, when the seeing or weather conditions do not meet our survey requirements, we will carry out the following backup observations: (1) Observe Deep and Ultradeep fields to supplement transient observations; (2) If it is clear but the seeing is bad, we will run multi-scale dithering observation for the calibration star fields to characterize the response (illumination) pattern over the field of view, and we will observe fields with short exposures to extend magnitude overlap with SDSS objects for photometric calibration.

8 Software and Calibration

8.1 Image processing pipeline

Our goal in processing the HSC images is to allow most science analyses to be carried out using the output catalogs containing the measured properties of detected objects, without requiring scientists to work with the images themselves. It was the SDSS experience that sufficiently sophisticated image processing allowed most science analyses to be done with the catalogs alone. The image processing pipeline needs to measure the properties (photometry, astrometry, object shapes, etc) of each detected object, to an accuracy limited by the depth and seeing of the data themselves, rather than by systematics in the processing or calibration. We have built a pipeline on the legacy of both the SDSS (Lupton et al. 2001) and Suprime-Cam (Furusawa et al. 2008), and are working closely with the Data Management Team of the LSST to share software tools and algorithms. We have carried out extensive tests of our pipeline using both simulated data, and archival SDSS and Suprime-Cam data.

Our requirements for the software are as follows:

- Absolute broad-band photometric calibration per exposure of 1% rms in each filter, uniform over the survey area. This is comparable to the delivered calibration accuracy of SDSS (Padmanabhan et al. 2008) and Pan-STARRS1 (Schlafly et al. 2012), and as we will have multiple dithered exposures to tie down the system, we are confident that we will reach this requirement. Stable and accurate calibration (Section 8.2) is key for WL analysis, photometric redshifts, large-scale structure studies, and studies of the physical properties of galaxies and stars.
- Astrometric calibration rms accuracy per exposure of 100 mas, allowing all astrometry to be tied together across the survey.
- Repeat observations of a given star should have an astrometric calibration rms error of 10 mas. This is

limited, in practice, by unmodeled distortions in the atmosphere. This requirement determines our ability to measure proper motions of stars.

- An accurate estimate of both the size and shape of the PSF is necessary to model its effects on galaxy shapes. Based on the expected S/N of our lensing measurements, we require that the PSF size (ellipticity) be measured to 0.3% (1% of typical values), which seems achievable based on current data.
- We can use simulations, analytic calculations, and the data themselves to constrain certain well-understood types of biases in galaxy shape measurements. We require that any remaining multiplicative calibration biases be below 0.6%, and that 98% of the typical PSF anisotropy be removed from the galaxy shapes.

We have already met and exceeded most of these requirements in processing simulated HSC data and archival Suprime-Cam observations, with a clear path to meeting the rest. We are basing our software framework on that of the LSST, which allows us to leverage the substantial effort of the LSST data management team. Like LSST, our challenge is to process in a uniform way multiple images of a given region of sky, and to optimally combine the detections on the individual exposures. We do so not by simply coadding the images, which would mix together data with a range of seeing, but rather by working with each exposure separately and carrying out a fit for the brightness, position, and shape of each detected object across all exposures simultaneously. This takes full advantage of the best-seeing data, properly propagates the noise properties of each frame, and keeps the noise on each pixel independent.

The PSF is measured from stars on each exposure, and a model for the spatial dependence of the PSF is fit (see Figure 13). This model is used for optimal photometry of stars, and is convolved with model galaxy profiles to fit galaxy properties. Convolving the image with the PSF allows optimal detection of objects. The stars detected are matched to SDSS for astrometric and photometric calibration (Section 8.2). Finally, for multiple exposures, each image is subtracted against a coaddition after convolving to a common PSF to search for variable objects in the difference image.

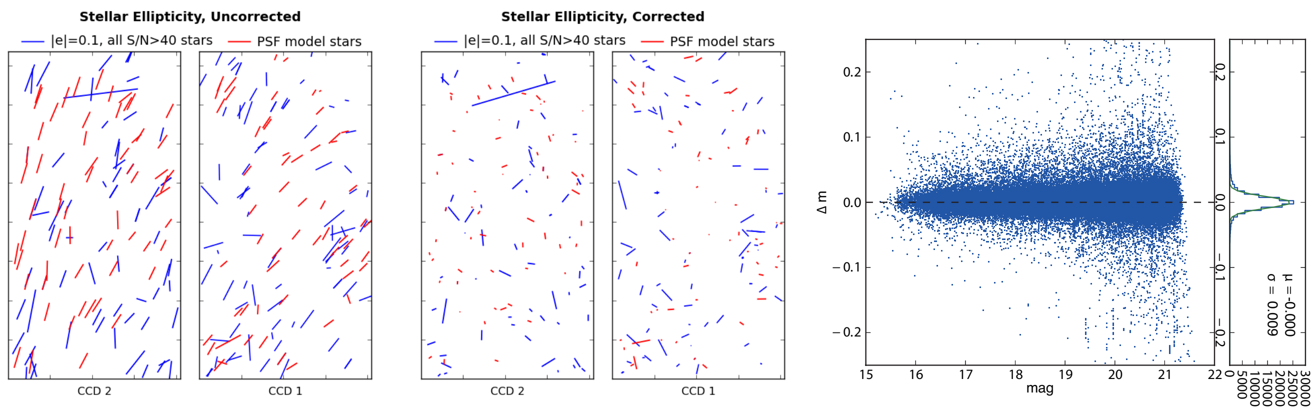

Figure 13: The ellipticity whisker plot for stars in two CCDs for a single exposure of z-band Suprime-Cam data before (*left panel*) and after (*middle panel*) subtracting the PSF model ellipticity. Stars used to determine the PSF and a fainter star sample are shown in different colors. This shows that stars can be used to make a PSF model that accurately traces the stellar ellipticities; the fainter star sample contains a few contaminating galaxies with highly discrepant ellipticities, but coherent PSF anisotropies are largely removed. Ongoing work will improve the modeling of the PSF further, to achieve the requirements for weak lensing. *Right panel:* The accuracy of relative photometry between multiple exposures in i of a single stellar field (observed with Suprime-Cam in August 2012) after application of the photometric calibration procedure described in Section 8.2. The rms difference is less than 10 millimag. This field was observed with multiple large dithers and rotations between the observations, as we will do with the HSC survey.

Each detected object will include measurements of its position, brightness (from PSF and galaxy model fitting, e.g., the right panel of Figure 13, as well as within a fixed aperture), scale size, ellipticity and other shape measurements, and estimated errors on these quantities. Information on variability or proper motion will also be reported. All these quantities will be stored in a database accessible to the collaboration. For the Deep and Ultradeep layers, we will provide preliminary reductions of the previous night's data for the identification of transient sources by HSC collaboration scientists.

A quicker version of the processing software will run at Subaru as images come off the telescope, which will provide the seeing and photometric zero-point in almost real time. This will allow the observers to make real-time decisions about observing conditions and what fields to image next. This information will be stored in the survey operations database to track the completeness of the survey.

A database will archive the scientific data products from the HSC survey (the processed image data for individual exposures and mosaiced and stacked images, as well as a comprehensive catalog of the measured properties of detected sources), and will support data retrieval by our team and the Japanese astronomical community via a dedicated web interface. To enable fast access by the co-I members, the data products will be mirrored at partner institutions.

8.2 Photometric and astrometric calibration of the survey

The photometric and astrometric calibration of HSC will be tied to that of SDSS, as the footprint of our proposed survey falls completely within that of SDSS. SDSS' photometry was calibrated to of order 1% (Padmanabhan et al. 2008); with our repeat imaging, and careful measurement of flat fields, we expect to be able to match this. We will use a natural photometric system—that is, one which is defined by the wavelength response of the HSC filter system. The magnitudes we produce will therefore be just the instrumental magnitudes normalized to AB zero points, derived from the SDSS. This is possible because of the expected stability of the HSC instrument (both the filters and the CCDs), whose wavelength response we will monitor through the survey with a dedicated instrument that can illuminate the focal plane with monochromatic light when the instrument is off the telescope.

We will take a 30 second exposure at each pointing in each filter to tie the HSC photometry to that of the much shallower SDSS at magnitudes $17 - 20$ (the default 3 minute exposures will saturate at $r \sim 19$, where the S/N of the SDSS photometry starts to drop). This will also be used to identify bright PSF stars for the deeper survey exposures. Given that we are tying to existing photometry, we can take data in mildly non-photometric conditions, as long as there is not too much spatial variation in the atmospheric extinction (cf., Ivezić et al. 2007). The HSC filter set is not identical to that of SDSS, but for main sequence stars, it will be straightforward to define color terms that allow us to tie the two together, including in the y band using model atmospheres and UKIDSS photometry. Given these model atmospheres, we can similarly define the zero-point of the narrow-band filters.

A changing water vapor column has the potential to affect the z and y response functions at the 2% level. We will use the real-time measurements of this column on Mauna Kea from JCMT and CSO to calculate and correct for this effect. The effect of water vapor should be smaller for HSC than for SDSS (because Mauna Kea is much drier than is APO), and given that this effect was undetectable in the SDSS photometry, we expect the effects to be small in the HSC survey as well.

Doing accurate photometry requires understanding the *internal* calibration of the instrument, i.e., the *ratios* of the sensitivities of each pixel on each detector to any other. This flat-fielding process is challenging, due to scattered light in flat-field data. The problem is especially pronounced for fast, wide-field systems like HSC, which are essentially impossible to fully baffle. We will generate monthly flats taken at zenith from the illuminated screen on the dome, taken always with exactly the same instrumental and telescope configuration, using lamps which mimic reasonably the SEDs of the bulk of the SDSS stars, about 4000K. The scattering contribution to these is spatially smooth and is stable by construction, and will be removed by fitting repeat stellar photometry over the field. We expect of order 600 stars per pointing, and results from different pointings can be combined to get superb statistics on the flat-field. Given our large dithers, the overlap between fields allows the flat-field to be constrained from repeat photometry of stars on different parts of the focal plane; these overlaps allow us to carry out an "uber-calibration", following Padmanabhan et al. (2008) and Schlafly et al. (2012).

To do really faint photometry, it is necessary to measure and subtract the sky very accurately, which is an entirely separate problem from the photometric flat-fielding. This will be done by constructing flattened sky templates (not "flats") by combining the data from many exposures, which will then be subtracted from an individual flattened data frame. These images will contaminated by scattered sky light, moonlight, etc, but our work with Suprime-Cam data shows that a principal component analysis of many sky frames works well, and takes out the fringing in the redder bands.

Astrometric calibration and stability can be checked by images in a few standard fields with a high density of stars. Repeat observations of these fields will also provide an independent check on the photometric stability, since any change in the response functions will produce changes in the relative instrumental colors for stars of different types/colors.

9 Concluding Remarks

Hyper Suprime-Cam, with its enormous field of view, and the superb image quality on one of the largest telescopes in the world, have achieved the most powerful imaging survey capability in the world. The cosmology and galaxy evolution science we propose to carry out is at the forefront of modern astronomical research, and will help maintain Subaru's position as the pre-eminent telescope in the world. The data will be processed with a state-of-the-art pipeline that will allow scientists to carry out their analyses at the catalog level.

The data will be distributed to the collaboration, to the Japanese astronomical community, and after a suitable proprietary period, to the world via a sophisticated database, that allows our far-flung collaboration to access the data simultaneously and work together on scientific projects. Our cadence has been designed to allow science to be done after the first year of data, stimulating our collaboration to work on science throughout the five years of the program, and drawing attention of the worldwide scientific community to our survey. We have organized ourselves in working groups around the broad science themes described in this proposal, which have developed plans and software tools for carrying out the analyses to reach the science goals. Our publications will be subject to a survey-wide data policy, with clear-cut guidelines on communication and authorship that encourage junior scientists to lead scientific projects and become first authors on the resulting papers.

In conclusion, the HSC survey will be the most powerful optical imaging survey of the decade, and promises to have a scientific impact comparable to that of the great imaging surveys of the past.

References

A. Albrecht et al., arXiv:astro-ph/0609591 (2006); T. Baldauf et al., PRD, **81**, 3531 (2010); P. S. Behroozi et al., ApJ, **717**, 379 (2010); V. Belokurov et al., ApJ, **642**, L137 (2006); G. Bernstein, & M. Jarvis, AJ, **123**, 583 (2002); J. Bernstein et al., ApJ, **753**, 152 (2012); J. Bosch, AJ, **140**, 870 (2010); K. Bundy et al., ApJ, **651**, 120 (2006); P. Capak et al., ApJS, **172**, 99 (2007); C. A. Collins et al., Nature, **458**, 603 (2009); L. L. Cowie, & A. J. Barger, ApJ, **686**, 72 (2008); S. Croom et al., MNRAS, **399**, 1755 (2009); E. Daddi et al., ApJ, **670**, 156, (2007); K. Dawson et al., arXiv:1208.0022 (2012); G. De Lucia et al., MNRAS, **366**, 499 (2006); G. De Lucia, & J. Blaizot, MNRAS, **375**, 2 (2007); J. Dunkley et al., ApJS, **180**, 306 (2009); R. Ellis, M. Takada et al., arXiv:1206.0737 (2012); X. Fan, C. L. Carilli, & B. Keating, ARAA, **44**, 415 (2006); S. Foucaud et al., A&A, **409**, 835 (2003); S. Foucaud et al., MNRAS, **406**, 147 (2010); H. Furusawa et al., ApJS, **176**, 1 (2008); L. Guaita et al., ApJ, **714**, 255 (2010); J. Gunn, & B. Peterson, ApJ, **142**, 1633 (1965); J. Guzik, B. Jain, & M. Takada, PRD, **81**, 3503 (2010); A. Hearin et al., ApJ, **720**, 1351 (2010); C. Heymans et al., arXiv:1210.0032 (2012); C. Hikage, M. Takada, & D. Spergel, MNRAS, **419**, 3457 (2012); C. Hirata, & U. Seljak, MNRAS, **343**, 459 (2003); G. J. Hill et al., SPIE, **7735**, 20 (2010); A. M. Hopkins, & J. F. Beacom, ApJ, **651**, 142 (2006a); P. F. Hopkins, et al., ApJS, **163**, 1 (2006b); E. Huff, & G. Graves, arXiv:1111.1070 (2011); H. Ikeda et al., ApJ, **728**, L25 (2011); O. Ilbert et al., ApJ, **690**, 1236 (2009); Z. Ivezić et al., AJ, **122**, 2749 (2001); Z. Ivezić et al., AJ, **134**, 973 (2007); M. Iye et al., Nature, **443**, 186 (2006); B. Joachimi, & S. Bridle, A&A, **523**, 1 (2010); N. Kaiser, G. Squires, & T. Broadhurst, ApJ, **449**, 460 (1995); J. S. Kartaltepe, et al., ApJS, **172**, 320 (2007); N. Kashikawa et al., ApJ, **648**, 7 (2006); N. Kashikawa et al., ApJ, **663**, 765 (2007); I. Kayo, M. Takada, & B. Jain, arXiv:1207.6322 (2012); M. Kurtz et al., ApJ, **750**, 168 (2012); A. Leauthaud et al., ApJS, **172**, 219 (2007); A. Leauthaud et al., ApJ, **744**, 159 (2012); K.-S. Lee et al., ApJ, **695**, 368 (2009); A. Lidz et al., ApJ, **690**, 252 (2009); S. Lilly et al., ApJS, **184**, 218 (2009); L. Lin et al., ApJ, **718**, 1158 (2010); J. Lotz et al., ApJ, **742**, 103 (2011); R. Lupton et al., ASP Conf. Proc., **238** , 269 (2001); J. P. Madrid, & D. Macchetto, arXiv:0901.4552 (2009); S. Malhotra, & J. E. Rhoads, ApJ, **617**, L5 (2004); R. Mandelbaum et al., MNRAS, **361**, 1287 (2005); R. Mandelbaum et al., MNRAS, **368**, 715 (2006); R. Mandelbaum et al., ascl:1108.002 (2011); R. Mandelbaum et al., arXiv:1207.1120 (2012); Y. Matsuda et al., MNRAS, **410**, L13 (2011); Y. Matsuda et al., MNRAS, **425**, 878 (2012); R. J. McLure et al., MNRAS, **395**, 2196 (2009); M. McQuinn et al., MNRAS, **377**, 1043 (2007); M. McQuinn et al., MNRAS, **388**, 1101 (2008); S. Miyatake et al., arXiv:1209.4643 (2012); S. Miyazaki, Y. Komiyama et al., PASJ, **54**, 83 (2002a); S. Miyazaki, T. Hamana et al., ApJ, **580**, L97 (2002b); S. Miyazaki et al., ApJ, **669**, 714 (2007); T. Morokuma et al., ApJ, **676**, 121 (2008); N. Mostek et al., ApJ, **746**, 124 (2012); B. Moster et al., ApJ, **710**, 903 (2010); T. Naab et al., ApJ, **699**, L178 (2009); J. Newman, ApJ, **684**, 88 (2008); M. Niemack et al., SPIE, **7741**, 51 (2010); A. J. Nishizawa et al., ApJ, **718**, 1252 (2010); K. Noeske et al., ApJ, **660**, L43 (2007); M. Oguri, & M. Takada, PRD, **83**, 023008 (2011); M. Oguri et al., MNRAS, **420**, 3213 (2012); N. Okabe, M. Takada et al., PASJ, **62**, 811 (2010); Y. Okura, & T. Futamase, ApJ, **748**, 112 (2012); Y. Ono et al., MNRAS, **402**, 1580 (2010); K. Ota et al., ApJ, **677**, 12 (2008); M. Ouchi et al., ApJ, **611**, 685 (2004); M. Ouchi et al., ApJS, **176**, 301 (2008); M. Ouchi et al., ApJ, **706**, 1136 (2009); M. Ouchi et al., ApJ, **723**, 869 (2010); N. Padmanabhan et al., ApJ, **674**, 1217 (2008); R. Reyes, R. Mandelbaum et al., Nature, **464**, 256 (2010); R. Reyes, R. Mandelbaum et al., MNRAS, **425**, 2610 (2012); G. Richards et al., AJ, **123**, 2945 (2002); G. Richards et al., AJ, **131**, 49 (2006); B. Robertson et al., Nature, **468**, 49 (2010); T. Saito et al., ApJ, **675**, 1076 (2008); S. Salim et al., ApJ, **700**, 161 (2009); M. Sato et al, ApJ, **701**, 945 (2009); E. F. Schlafly et al., ApJ, 756, 158 (2012); M. Shirasaki et al., arXiv:1204.4981 (2012); D. Spergel, ApJS, **191**, 58S (2010); C. Steidel et al., ApJ, **736**, 160 (2011); M. Strauss et al., ApJ, **522**, L61 (1999); M. Strauss et al., AJ, **124**, 1810 (2002); N. Suzuki et al., ApJ, **746**, 85 (2012); M. Takada, & B. Jain, MNRAS, **348**, 897 (2004); R. Takahashi et al., ApJ, **700**, 479 (2009); R. Takahashi et al., ApJ, **726**, 7 (2011); T. Tal, & P. G. van Dokkum, ApJ, **731**, 89 (2011); J. Tang, I. Kayo, & M. Takada, MNRAS, **416**, 2291 (2011); Y. K. Uchimoto et al., PASJ, **60**, 683 (2008); T. Valentinuzzi et al., ApJ, **721**, L19 (2010); P. G. van Dokkum et al., ApJ, **677**, L5 (2008); M. White et al., ApJ, **728**, 126 (2011); D. G. York et al., AJ, **120**, 1579 (2000); S. Zaroubi et al., MNRAS, **425**, 2964 (2012); J. Zhang, MNRAS, **383**, 113 (2008).